Politecnico Di Milano
Scuola di Ingegneria Industriale e dell'Informazione

Corso di Laurea Specialistica in Ingegneria Fisica
Indirizzo Nano-Ottica e Fotonica

A Study of the Damaging Process in Europium-doped $BaAlMg_{10}O_{17}$

Tesi Magistrale di
Andrea Del Prete

Relatore Giacomo GHIRINGHELLI

Correlatori Pieter GLATZEL
Lucia AMIDANI

Sessione Laurea Aprile 2016
Anno Accademico 2014/2015

Abstract

The present work has been carried out at the European Synchrotron Radiation Facility (ESRF) in the High-Brilliance X-Ray Spectroscopy beam-line ID26 under the supervision of Pieter Glatzel and Lucia Amidani. The topic is the study and simulation of spectroscopic data concerning the crystal phosphor $BaMgAl_{10}O_{17}$ doped with Europium or Manganese or both. Despite the high luminescence yield gained with the inclusion of the two metals, the material faces damaging when exposed to heating or irradiation. The aim is to identify the main physical phenomenon underlying the loss in luminescence starting from the two most cited in literature: oxidation of Europium and structural changes in the crystal.

Two main techniques of analysis will be employed: a statistical tool, named Principal Component Analysis, and the first-principle simulation of spectral features. The first will be addressed to the study of an irradiation-related dataset, while the second will both try to calculate electronic structures and assess the reliability of the two software by comparing their results.

Sommario

Il presente lavoro è stato svolto a Grenoble presso ESRF (European Synchrotron Radiation Facility) sotto la supervisione di Pieter Glatzel e Lucia Amidani. L'obiettivo è lo studio e la simulazione di dati spettroscopici riguardanti il cristallo $BaMgAl_{10}O_{17}$ drogato con Europio (BAM:Eu) o Manganese (BAM:Mn) o entrambi (BAM:Eu, Mn).

La peculiarità di tale materiale (considerando la froma drogata con Europio, la più interessante) è la forte luminescenza blu a seguito di irraggiamento UV. Il processo di luminescenza avviene grazie all'assorbimento di luce da parte del reticolo cristallino, a cui segue un trasferimento di energia verso l'atomo di Europio o Manganese per via radiativa oppure tramite ricombinazione di coppie elettrone-lacuna. Il colore della radiazione emessa è caratteristico della transizione $5d \rightarrow 4f$ dell'Europio, la cui energia risulta variata dagli effetti del reticolo circostante.

Il cristallo, una volta drogato con Europio, presenta caratteristiche ottimali per essere utilizzato come fluoroforo blu ad alta efficienza in applicazioni come lampade, schermi al plasma e LED bianchi. Tuttavia, la vita utile di tali dispositivi è limitata da problematiche connesse al danneggiamento del cristallo: irraggiamento (sia nello spettro UV sia in quello X) e surriscaldamento contribuiscono a limitare l'emissione di luce nella lunghezza d'onda di interesse.

Tramite irraggiamento X si spera di simulare lo stesso effetto indotto dalla luce UV, rendendo possibile lo studio del processo di danneggiamento dal punto di vista della struttura elettronica nel momento stesso in cui esso avviene. Questo fornirebbe all'industria uno strumento affidabile per la comprensione del fenomeno di decadimento della luminescenza.

Tra le cause attualmente riportate in letteratura figurano l'ossidazione dell'Europio e la possibilità di uno spostamento di quest'ultimo dal sito di sostituzione verso altre posizioni stabili. Entrambi i processi determinano una riduzione in efficienza dello scambio energetico tra reticolo e atomo ospite, limitando così anche la quantità di luce emessa.

Nella presente tesi si cerca di comprendere quale di questi fenomeni fisici risulti determinante nel processo di danneggiamento. Per fare ciò si è utilizzato uno strumento di analisi statistica, detto Analisi delle Componenti Principali (PCA), e la simulazione degli spettri misurati tramite i software `FEFF9` e `fdmnes` .

Nel Capitolo 3 verrà illustrata sia la teoria alla base della PCA, sia la sua applicazione a un insieme di dati relativi al progressivo danneggiamento da raggi X. Tale danneggiamento si manifesta, alla soglia L dell'Europio, come un abbassamento del picco principale a favore di uno inizialmente di minore intensità. L'obiettivo è determinare il numero minimo di componenti che può originare, tramite una combinazione lineare, l'intero insieme di dati e le variazioni in esso presenti. La risposta fornirebbe indicazioni sul tipo di processo fisico alla base del danneggiamento, sia che questo sia rappresentato da una ossidazione o da un cambiamento strutturale nel cristallo.

Nel Capitolo 4 verranno descritti i due software utilizzati e i risultati da essi ottenuti. Per le simulazioni sono stati considerati sia alcuni campioni di riferimento sia il materiali in sé, nella forma drogata e non. Gli spettri ottenuti permettono deduzioni coerenti con quanto si trova in letteratura e, in più, un confronto sulla qualità dei risultati tra i due software.

Acknowledgements

First of all I would like to thank Pieter Glatzel and the current ID26 team at the ESRF: they made this work possible both by accepting my candidature and by being supportive throughout the six months. In particular, Lucia Amidani has been following up close the whole project and has given me valuable feedback about the content of the thesis. Her suggestions had a huge impact on the shape of the work and helped make the topic clearer to someone who had never dealt with fluorescence and X-Ray spectroscopies.

Among those that I got to know in this period, I want to thank Alessandro Smareglia: his seemingly unlimited reservoir of coffee proved to be useful to make up for the time lost in our programming-oriented coffee-breaks.

Besides all this, the biggest thanks goes to my family and my girlfriend, Sara Ghielmi: their support has been crucial both before leaving for France and during my stay. Without their push to look also abroad for a thesis project, this exchange would have not been possible.

Many others have played a role in this half-year in France; a list with all of them would be a difficult and long task and hopefully they will be happy with the knowledge of having given me a hand.

Contents

List of Figures

List of Tables

Chapter 1

The Scientific Case

1.1 BAM: the subject of the study

1.1.1 The Crystal Structure

BAM is a crystalline material with stoichiometric formula $BaMgAl_{10}O_{17}$ and β-alumina structure. The salient feature of this structure is its two-dimensional character: the crystal is made of parallel thin layers of dense alumina (the *spinel block*) separated from each other by scarcely occupied planes (the *mirror* or *conduction layer*) where all Barium ions are confined.

The *spinel block* is made by a lattice of Aluminium atoms surrounded by Oxygen both in tetrahedral and octahedral configuration. Magnesium also finds its place in this part of the crystal.

The *conduction layer* in entirely made up of alternating Barium and Oxygen. Its name comes from its usage in classic β-alumina, where it can act as a channel for the migration of ions thanks to the oxide framework.

The unit cell belongs to the space group $P63_{mmc}$ with lattice constants $a = b = 5.6255$ Å, $c = 22.6587$ Å, $\alpha = \beta = 90$ and $\gamma = 120$ degrees.

The production process involves doping of $NaAl_{11}O_{17}$ with Barium and Magnesium, in which the former takes the place of Sodium and the latter takes the place of Aluminium in tetrahedral sites. The charge neutrality of the unit cell is preserved: Na^{+} becomes Ba^{2+} and Al^{3+} becomes Mg^{2+}, with 2 Ba and 2 Mg

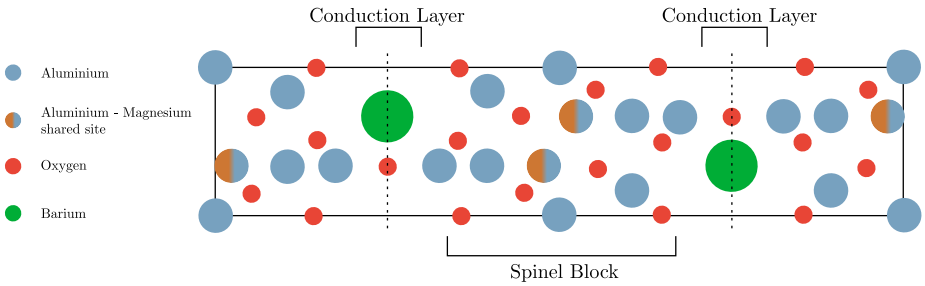

Figure 1.1: Side view of $BaMgAl_{10}O_{17}$ unit cell.

present in every unit cell.

The structure gains more interesting properties (among which there is luminescence, the most important) when doped with Europium and Manganese (in this cases the material will be indicated with BAM:Eu or BAM:Mn). Eu takes the place of Barium in the conduction layer, but it seems to be able to move around thanks to the previously mentioned characteristic of the mirror layer. Mn has a more stable site in the spinel block, substituting for Mg^{2+} and keeping the same oxidation state. Doping is usually between 0.1% and 10% with respect to the number of possible substitution sites.

1.1.2 Optical Properties

The optical properties of BAM change dramatically when considering the two doped versions. The rare earth atom has the role of a blue light emitter that, once inserted in the host, gives off fluorescence with a high quantum yield. Manganese doped BAM is instead a green phosphor that becomes even more efficient if some atoms of Europium are also present.

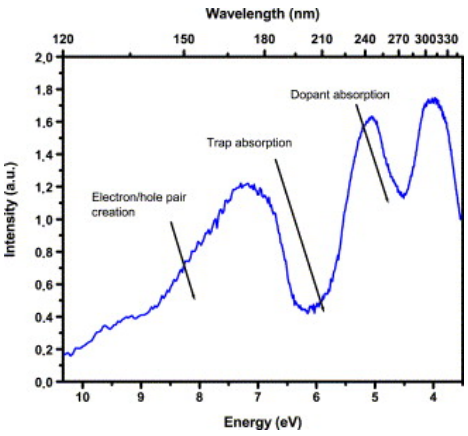

Figure 1.2: Excitation spectrum of BAM. The three excitation processes are associated with different features and the two rightmost peaks are due to the direct absorption to the split $5d^1$ state. Image source is Bizarri and Moine [4]

In the case of BAM:Eu the excitation can either be direct or mediated by the host. UV light is directly absorbed by the dopant, while VUV and X-Ray light are absorbed by the crystal structure and then transferred to the emitter. The emission of blue light is due to the dipole allowed transition from the excited state $4f^6 5d^1$ to the ground state $4f^7$ of Eu^{2+}.

More generally, among rare-earth-based phosphors there are two main processes that allow fluorescence: (1) dipole forbidden $f - f$ transitions, for example in Y_2O_3:Eu^{3+}, and (2) dipole allowed $f - d$ emission, of which the present material is an example [32]. In the first case the emission spectra presents sharp lines whose wavelength and intensity are almost independent from the host material, while in the second case there is broadband emission and a strong dependence on the host.

When considering the particular case of BAM:Eu, the second process relies heavily on the splitting of the Eu $5d$ orbitals due to effect of the crystal field. While f orbitals are well shielded by s and p electrons, d orbitals are severely affected by their surroundings. In the case of Eu^{2+}, when considering the free ion, the two first excited states are the $4f^7$ (in configuration $^6P_{7/2}$) and the $4f^6 5d^1$, the latter having higher energy. The effect of the neighbouring atoms is the twofold splitting of the $5d$ orbitals in the e_g and t_{2g}, in which the t_{2g} ends up in having less energy than the $4f^7 - {}^6P_{7/2}$ state (see Figure 1.3). In this situation the previously cited $d-f$ transitions is favoured and can be even tuned to a particular wavelength by changing the host lattice (that is, the intensity of

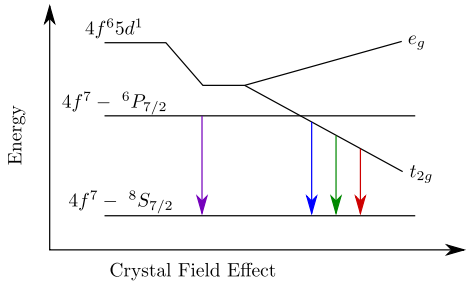

Figure 1.3: Variation in energy in f-transition metals states when tuning the effect of the crystal field

the crystal field).

Absorption depends on three main processes [4]: (1) direct and very efficient excitation of the dopant, (2) excitation to the minimum of the host conduction band and (3) creation of electron-hole pairs in the host. In the last case, to have an energy transfer to the ion, the electron-hole pair has to migrate to the site of the dopant and there recombine radiatively.

Another excitation mechanism is proposed by Howe and Diaz [21]: emission by the host lattice has remarkable overlap with the direct excitation modes of Eu^{2+} above 230 nm, suggesting the possibility of radiative energy transfer between the host and the dopant. It is not clear, unfortunately, the entity of this process when compared with the previous, although the authors of the paper suggests it could be a significant, if not the primary, mechanism of energy transfer.

1.1.3 Typical Applications

Despite being known for a long time (scientific research on the topic dates back 100 years), phosphors have gained interest in the past years thanks to the impulse given by new technologies. Plasma dislpay panels (PDP) were among the most important applications, requiring fluorescent crystals with high efficiency and long term stability. Here BAM:Eu plays a central role, having the perfect emission characteristics for an optimal performance in a PDP [3]: high quantum efficiency, good chromaticity and strong absorption under VUV light.

Other applications are fluorescent lamps, in which a phosphor is excited by the VUV light emitted by a mixture of Xenon and Neon. A better knowledge of materials like BAM:Eu is fundamental for phosphor optimization and thus more efficient lamps.

More generally, phosphors of colors other than blue can be used for white LED. For example, a coating of YAG:Ce^{3+} is able to absorb part of the light emitted by a blue LED and diffuse it as yellow light. The sum of transmitted blue and yellow makes a tunable white source, whose color temperature can be adjusted to warm (more yellow) or cold (more blue).

1.2 Open questions

Even though BAM has some remarkable properties, in the long term operation there are stability issues that manifest themselves as a loss in light emission. It is widely accepted that the two main causes to fluorescence degradation are thermal treatment in the manufacturing process and VUV irradiation during the lifetime of the phosphor [3, 41, 23, 8].

These two processes are supposed to influence either the position or the oxidation state of Europium, thus destroying the possibility of energy transfer between the host lattice and the dopant. It is hence of major interest to understand the crystal structure of the doped crystal and, in particular, the position occupied by Eu, for example via X-Ray diffraction studies [28].

There are less unknowns when dealing with Manganese as its position in the spinel block is fairly stable. Its green fluorescence depends on the amount of co-doping with Europium and the relation between the two rather well understood.

On Barium there are no open problems since its position in the structure is surely in the conduction layer and there are no hints of it moving around. Its electronic structure should be sensible to what happens in the mirror layer and, as a matter of fact, the spectra taken at the beamline show some dependence on the doping with Europium or Manganese. This problem will be addressed later in Section 4.2.3.

1.3 Consolidated answers

So far multiple explanations have been put forward in order to describe the physics beneath the loss of luminescence in BAM:Eu. Formation of magneto-plumbite phase, oxidation, migration of Europium and creation of traps are all among the ideas.

For example, Lambert et al. [28] have shown that X-Ray diffraction is able to detect Europium in multiple positions in addition to the classical Barium site. The identified sites are four and are given the following names: Beaver Ross site (the position of Barium), anti-Beaver Ross site, (near-)middle-Oxygen site and near-Oxygen site (see Figure 1.4). The possible shift of the atoms would ruin the energy transfer between itself and the host-lattice.

The process of Eu oxidation has been seen via XPS measurements [44] and by XANES [18]. When considering Eu in the position of Barium, it is easy to assume that the empty space present in the conduction layer favours the movement of O_2 and H_2O, thus enabling the reduction of the dopant. This process is triggered by the Oxygen present in air during the production of the luminescent material or during annealing (done to simulate the production process of plasma display panels) [3]. As a matter of fact, experiments by Liu et al. [30] of synthesis of BAM:Eu in air, neutral or reducing atmosphere (N_2 and N_2 plus H_2) have shown that the amount of oxidized Eu is highest in the first case.

Despite the role of the Oxygen in the atmosphere, also self-oxidation of Europium is possible [23]. This seems to be mostly the case with VUV irradiation: when considering this kind of light, some Oxygen in the mirror layer might disappear, leaving a so-called Oxygen vacancy V_O. This vacancies (quite near to Europium sites) act as traps for electrons from the dopant, thus allowing existence for Eu^{3+}.

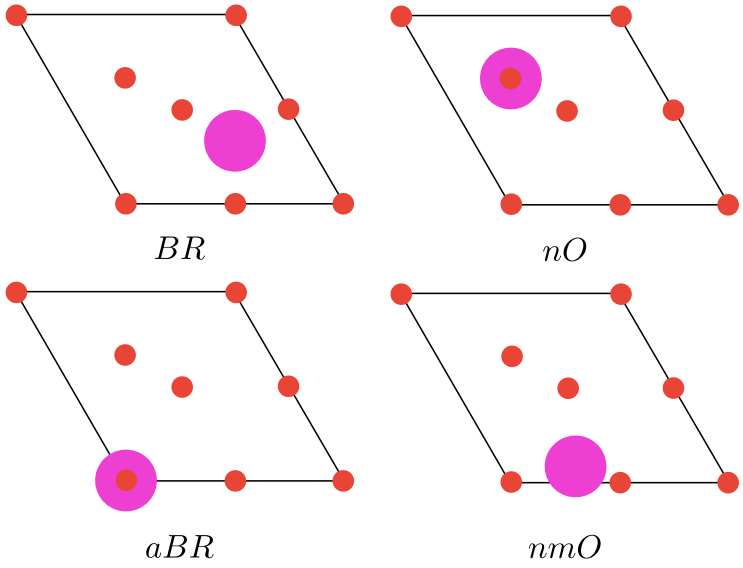

Figure 1.4: Top view of the four possible sites for the Europium, after the damaging process. Only the nO position is not on the mirror plane, but is 0.42 Å off.

The role of traps is to destroy the energy transfer mechanism by intercepting electrons or holes before they can recombine on the dopant atom. The traps absorption band is seen to increase during the damaging process, thus indicating an increase in their density. It seems that no new kind of trap is created; rather, even the newly created ones are the same as those due to the synthesis of the material [3].

As said before, there are two main causes of damage in the lifetime of fluorescent BAM: thermal exposure and VUV irradiation. Both concurr to oxidation, but the first seems to add the movement of Europium, while the second the formation of traps in the crystal structure. A difference in the oxidation process has been pointed out by Jia-Chi, Mei-Jiao, and Yu-Hua [23]: the transition $Eu^{2+} \rightarrow Eu^{3+}$ is mostly self-induced when caused by VUV light; this is proved by the fact that the phenomenon happens even when the whole process of synthesis and irradiation is carried out in Nitrogen.

Other sources of damage in PDP (electronic, ionic and neutral species sputtering) have been ruled out by Bizarri and Moine [3] as having a negligible effect on the luminescence.

Chapter 2

Experimental Techniques

2.1 XAS and XES

X-Ray techniques are based on two fundamental light-matter interactions: photoelectric absorption and scattering. In XAS (X-Ray Absorption Spectroscopy) the light transmitted from a sample is measured, while in XES (X-Ray Emission Spectroscopy) the object is fluorescent emission. The properties of the incoming and outgoing beam (intensity I, energy E and momentum $\mathbf{k}$) are either measured or known and from possible differences between the initial and final values, useful insight is gained on the physical and optical properties of the studied material. In particular, the term "spectroscopy" is referred to the cases in which there is a non-zero exchange of energy ($E_i \neq E_f$).

In this part the focus will be on the physical processes that make X-Ray spectroscopy possible; for a summary of a typical experimental setup Section 2.3 on page 14 will suffice.

The transmission of light through a opaque material is governed by the Lambert-Beer law $I_{out} = I_{in} \exp(-\mu z)$ where z is the direction along the beam and μ is defined as the *linear absorption coefficient*. The aim of a spectroscopic experiment is to measure I_{out} and I_{in} as a function of energy in order to evaluate the function $\mu(E) = \frac{1}{z} \log \frac{I_{in}}{I_{out}}$.

The analysis of $\mu(E)$ in the X-Ray region shows a behaviour peculiar of each atomic element: an overall monotonic decreasing dependence on E interrupted by sharp raising edges at well defined energies (see the left part of Figure 2.1a) followed by wiggles and oscillations fading out within hundreds of eV from the edge. The position, intensity and shape of these edges allows for the identification of atoms and their surroundings, plus information on the ionization state and electronic structure.

The connection between μ and atomic properties is mediated by the atomic cross-section σ: the absorption coefficient can be written as $\mu = \sum_i \sigma_i n_i$ where i identifies an atomic species with density n_i. Then, σ is seen to depend on the scattered forward intensity $f(0)$ (which can be calculated via quantum mechan-

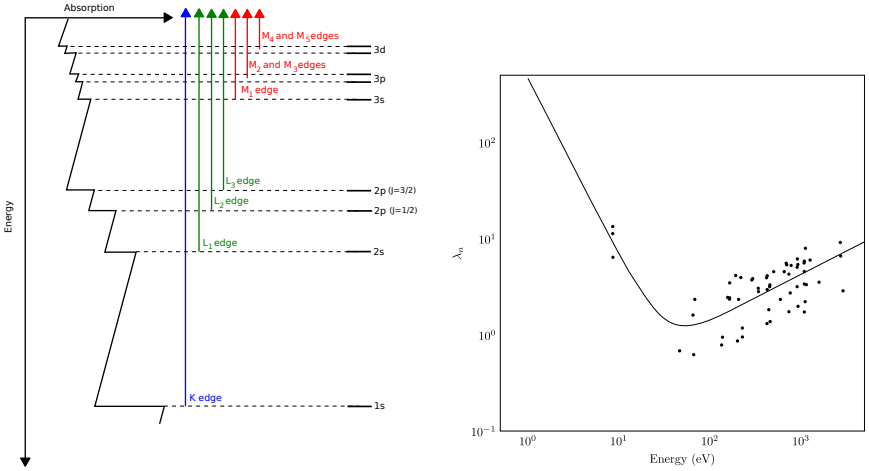

(a) *Available transitions from core shells and relative edges in the absorption coefficient. Image from Wikipedia.*

(b) *Electron mean free path in different materials. Reproduced from [39]*

Figure 2.1

ical arguments) thanks to the *optical theorem*:

$$\sigma = \frac{4\pi}{k}\mathrm{Im}[f(0)] \qquad \text{in the simple case of a plane wave} \tag{2.1}$$

In the range of energies of interest, the behaviour of μ is dominated by the photoelectric absorption from core hole electrons towards excited states in the continuum or just below the Fermi energy. Each of the edges in μ corresponds to the excitation of an electron from a different core shell, its position being determined by the difference in energy between the initial and final state. The nomenclature of the edges follows that of the shells: thus, K, L and M edges refer to electrons excited from $n = 1,\ 2$ and 3 orbitals, L_I, L_{II} and L_{III} to the angular orbitals $2s, 2p_{1/2}$ and $2p_{3/2}$ and so on (as seen in Figure 2.1a).

After the excitation, the atom is not stable and relaxes after a time $t \simeq \frac{\hbar}{\Delta E}$ via X-Ray fluorescence or Auger electron emission (here, ΔE is the uncertainty on the energy of the final state). These secondary transitions are also characteristic of the element and can be used for fingerprint identification.

A typical absorption edge is conventionally separated in two different parts: the *near edge* and the *extended fine structure*, the main difference being the possible energy of the incoming photon. This difference is in turn found in the energy of the photo-electron. In the first case the core electron is excited to a bound state near the Fermi level or slightly above it, and thus is still either inside the atom or in the continuum with very little kinetic energy. In the second case, the energy transfer to the photo-electron is considerably bigger: the electron finds itself in the continuum with a huge amount of kinetic energy.

This difference in kinetic energy accounts for the peculiar behaviour of the electron and the different range in which its wavefunction scatters. The mean free path is strongly dependent on the energy (see Figure 2.1b) and this allows the near edge or extended spectroscopy to probe respectively a bigger or smaller cluster around the absorbing atom.

2.1.1 XANES

XANES stands for X-Ray Absorption Near Edge Spectroscopy and covers the first part of the spectrum within 50 eV of the edge. It has now become a standard tool in chemical analysis thanks to its sensitivity to the lowest lying unoccupied states, the local symmetry and the oxidation state, but its interpretation is far from being standard and straightforward.

The probability of a transition of the excited electron to a different orbital is expressed by a matrix element involving the initial and final state and the transition operator. It follows that the considered states have to obey selection rules in order to give a non-zero probability. Thus K edge spectroscopy will probe mostly $1s \rightarrow np$ transitions, L edge spectroscopy will probe s and d states and so on. The main contribution is due to dipole transitions (± 1 in angular momentum) but there could be features dominated by quadrupolar transitions. The *pre-edge* present in some spectra is an example.

If the electron is excited to the continuum, its mean free path has to be considered. Since at low kinetic energies the space travelled by the particle can be huge, the electron goes through many scattering events with the surrounding atoms and probes a large cluster around the absorber. It is thus said that in the XANES region, i.e. where the kinetic energy of the photo-electron is low, the main physical phenomenon determining the spectrum is the *multiple scattering*. This is also the reason why in the spectrum there is information about the local symmetry around the absorbing atoms: the electron gathers this information by the multiple scattering events.

The sensitivity to oxidation states is shown as a shift in the position of the edge; in particular, there is an increase in the edge energy when considering more oxidized atoms. Unfortunately, it is not straightforward to apply this rule of thumb, since there are many other effects at play: inter-atomic distances, bond angles and ligand atomic charges all influence the spectral features.

The origin of the shift can be easily explained with an electrostatic model: higher oxidized states require more energetic X-Rays due to the less shielded (and thus more charged) atomic nucleus. An alternative explanation is due to the reduced absorber-scatterer distance when considering oxidized atoms, following the proposed empirical law [33] $\Delta E \approx 1/r^2$ for the features energy position. In this case a high oxidation state implies a shortening of bond distances and, in turn, higher energies.

2.1.2 EXAFS

EXAFS stands for Extended X-Ray Absorption Fine Structure and refers to the second part of an absorption spectrum, up to 1 keV from the edge. In this case the electron is excited to the continuum and the main physical process is the scattering of the wave function with the nearest neighbours.

Since the kinetic energy is high, the mean free path is small and the particle has not the opportunity to scatter on more than one atom. The resulting signal is the interference of multiple waves originating from different sites around the absorber. Changing the photon energy means changing the wavelength of the electron and thus meeting the conditions of constructive or destructive interference. This phenomenon is at the basis of the oscillations present in the

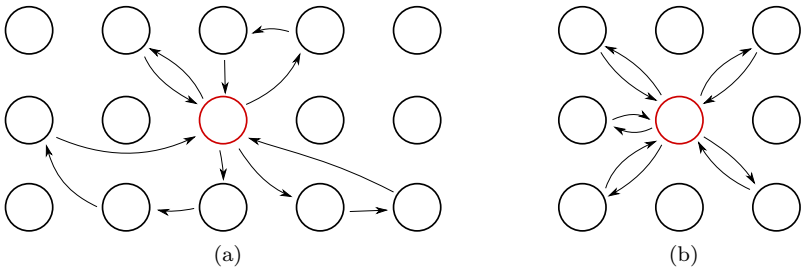

Figure 2.2: Representation of the different physical phenomena in XANES (a) and EXAFS (b)

absorption coefficient.

The EXAFS signal is modelled as a sum of sinusoidal functions originating from the scattering:

$$\chi(k) = -\frac{1}{k}\sum_{i=1}^{N} A_i(k)\sin(2kR_i + \phi_i(k)) \tag{2.2}$$

where A_i is the scattering amplitude from each neighbour, $\phi_i(k)$ is a phase term due to the scattering and k is the photo-electron wave number.

After subtraction of the background, the frequencies of the oscillations in the EXAFS spectra can give information on the positions of the scattering atoms while the amplitudes can be useful to determine their number. In general, the analysis of the former is more challenging, as in spectroscopy energy positions can be measured with higher precision that intensities.

2.1.3 XES

X-Ray Emission Spectroscopy studies a secondary process that follows the electron excitation, that is, the emission of a photon when an electron fills the core hole. This electron may come from a valence or inner shell and carry with itself chemical information about the atom, giving XES an element and site-specific character.

Depending on the origin of the electron, the spectroscopy is called *valence to core* (v.t.c) or *core to core* (c.t.c.), the latter having chemical sensitivity thanks to indirect effect like screening of the core potential.

When considering 3d-transition metal complexes, $K\beta$ lines (see Figure 2.3 for the nomenclature) are often used to identify the ligands and study the valence orbital structure. These spectra are split in different regions called $K\beta_{1,3}$ (also known as $K\beta$ main lines for their strong intensity), $K\beta''$ and $K\beta_{2,5}$; only the last two are part of the v.t.c. emission and can be used efficiently for ligand identification [12].

In particular $K\beta''$ transitions arise mainly from ligand s orbitals while $K\beta_{2,5}$ emerge from ibridization between ligand and metal p orbitals. For example, vtc-XES has been used to identify type and distance of ligands with similar atomic number (such as O, N and C), giving information unavailable to EXAFS [2].

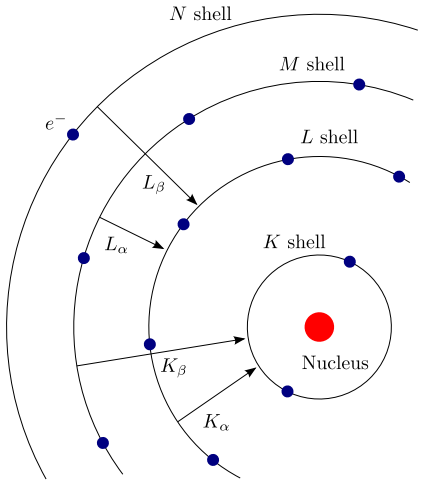

Figure 2.3: XES emission lines.

HERFD-XAS

X-Ray fluorescence can also be used to reduce the lifetime broadening in XANES and EXAFS measurements by looking at the emitted light in a narrow energy bandwidth [1]. This technique is called High Energy Resolution Fluorescence Detected XAS [14, 38] and its first proposed application dates back to 1991 [16].

The idea is to select a particular emission energy (possibly with high fluorescent yield) from the element of interest and then scan the absorption edge: in this case the spectral broadening is determined by the lifetime of the intermediate state (which is usually longer than that of a state with a core hole) and this allows to record a sharper spectra with better separated features.

For example, when considering core holes, the uncertainty in energy is a function of Z and ranges from 1 eV to 40 eV for K shells (Z from 23 to 40) and from 3.7 eV to 7.4 eV for L_{III} shells (Z from 60 to 92) [27]. In this situation, the energy resolution is no more determined by the beam quality. With the application of HERFD spectroscopy, sub-eV resolutions are achievable, as reported in De Groot, Krisch, and Vogel [9], where the authors provide the following equation to estimate the final lifetime broadening:

$$\Gamma_{tot} \approx \frac{1}{\sqrt{(\frac{1}{\Gamma_i})^2 + (\frac{1}{\Gamma_f})^2}} \tag{2.3}$$

where Γ_i and Γ_f are the intermediate and final state lifetimes.

This technique relies on the fact that, in the hard X-Ray range, the radiative decay is to a very good approximation proportional to the absorption coefficient. Unfortunately, one-electron theories are not always sufficient for a good description of the spectra and some conditions have to be met in order to affirm a correspondence between HERFD and XAS results [13]: (1) core hole potentials in the intermediate and final state should be similar and (2) electron-electron interactions between the core hole and the photo-excited state should be small.

2.2 The Synchrotron

In this section we will see not only how X-Ray light is produced in a synchrotron, but also why this kind of radiation is very different from what can be obtained for example in a more common hospital X-Ray source. These differences make a synchrotron light source an invaluable tool for scientific research.

The production of X-Ray radiation relies on the following physical phenomenon: when an electron (or any other charged particle) is accelerated, it emits electro-magnetic radiation at a frequency which depends on the acceleration itself. Placing the electrons on a circular path means that there always is a centripetal force applied on the particle: in this particular case the light is called synchrotron radiation.

A synchrotron facility is more generally aimed at accelerating charged particles and only in some cases electrons are used to exploit the by-product that is light. Depending on the application, the loss of energy due to emitted radiation can also be a drawback; this is the case at the LHC for particle physics studies. This kind of facilities is usually composed of (1) an injection system, where the particles are produced, (2) a booster synchrotron, where the particles are accelerated, (3) a storage ring, where the beam is kept in circulation, and (4) beamlines, where the X-Ray radiation is used to carry out experiments. All these elements can be seen in Figure 2.4 and are better explained below, taking as an example the structure of the ESRF.

The *LINAC* or *injector* contains an electron triode gun and a first accelerating stage; the gun works by heating a metal plate between a cathode and anode with high potential difference (in the order of hundreds of keV) in order to pass the electrons to the booster stage.

The *booster* is responsible to bring the electrons energy in the GeV range before injecting the particles in the storage ring. This is achieved with carefully synced radio-frequency (RF) cavities where an oscillating electric field gives a push to the incoming electrons. The frequency (and phase) of the cavity has to be carefully tailored: it has to be in sync with the passing of the beam, otherwise the desired accelerating effect might not be achieved. This is the phenomenon that gives the name to the whole facility. The role of the RF cavity is not only to accelerate the electrons: their function (both in the booster and in the storage ring) is also to remove the electrons that, within each bunch, due to dispersion, fall outside the required kinetic energy range. This is an additional cause of loss in the rings, but allows to have better shaped pulses.

The *storage ring* is the largest sector of a synchrotron facility; it has a pseudo-circular shape and is composed of RF cavities, bending magnets, undulators, quadrupoles and sextupoles. The last two devices are used for focusing and aberration correction, while the first two are used to produce X-Rays. In this case the RF cavities are used to restore the energy lost due to the irradiation.

Since the electrons will travel millions of kilometres and are known to scatter very easily, any gas residual will result in many collisions and consequently huge energy losses. For this reason the entire path along the electron beam has to be in ultra high vacuum (that is, less than 10^{-9} mbar).

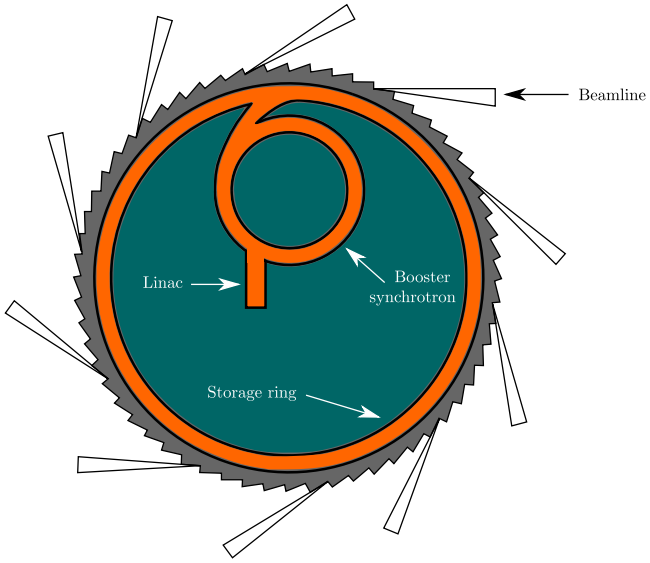

Figure 2.4: Graphical representation of a synchrotron light source

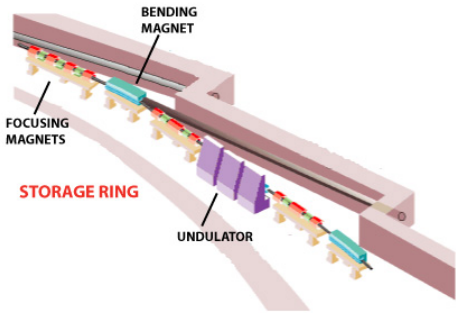

Figure 2.5: A section of the storage ring showing the *Bending Magnets* and the *Undulators*. Here are shown also the focusing magnets, described in detail below.

Light from acceleration

The storage ring is not really a perfect circle; it is instead made of straight and curved elements used for different purposes. Among these elements, the two aimed at X-Ray light production are the *Bending Magnets* and the *Undulators* (see Figure 2.5).

The *Undulators* (see Figure 2.7b) are devices made of an array of small magnets of alternating polarization that guide the electron on a undulating trajectory. On each bend the electron emits X-Rays and the light produced along all the device overlaps and interfere constructively. This allows for the generation of highly brilliant beams with photon energies concentrated on particular frequencies (and their harmonics); these frequencies can be fine tuned by changing the distance between the magnets.

The origin of the highly collimated beam is due to the Lorentz transformation

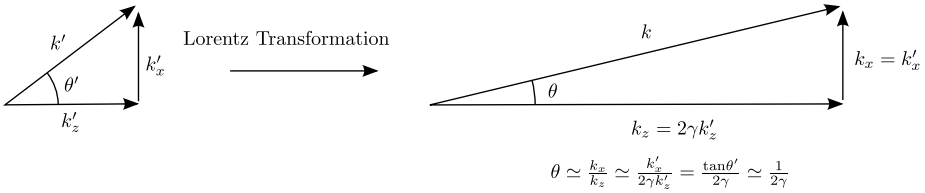

Figure 2.6: The Lorentz Transformation allows for a reduction of the divergence angle of a factor $\frac{1}{\gamma}$. Here z is the direction tangent to the circular path of the electron and $\mathbf{k}$ is the outgoing wave vector.

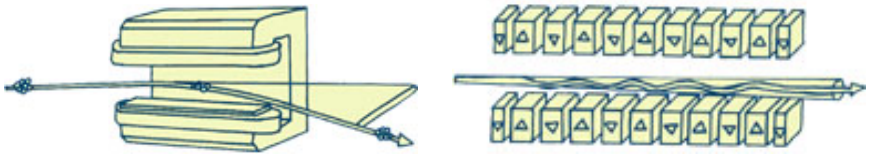

(a) *Bending Magnets.* (b) *Undulators.*

Figure 2.7

to take into account when considering a relativistic electron. The change in frame of reference (from the electron to the laboratory) also changes the shape of the emitted beam. In the fixed frame of the observer the dimension along the electron beam is dilated, while the perpendicular dimension is not affected: splitting the wave vector $\mathbf{k}$ of the outgoing X-Rays into its components k_z and k_x clearly shows that only k_z is changed, thus resulting in a narrowing of the divergence angle θ (see Figure 2.6).

The *Bending Magnets* (see Figure 2.7a) are mainly used to bend the beam and keep it in its orbit. These objects are dipole magnets that produce a homogeneous magnetic field along their distance. Following the Lorentz force $\mathbf{F} = \frac{d\mathbf{p}}{dt} = -e\mathbf{v} \times \mathbf{B}$ and considering a relativistic electron with momentum $\mathbf{p} = \gamma m\mathbf{v}$ and energy $E = \gamma mc^2$, the equation for the bending radius is:

$$\begin{aligned} \frac{d\mathbf{p}}{dt} = \gamma m \frac{d\mathbf{v}}{dt} &= -e\mathbf{v} \times \mathbf{B} \\ \gamma m(-\frac{v^2}{R}) &= -evB \\ R &= \frac{\gamma mv}{eB} \end{aligned}$$

As the electrons are bent away from their initial trajectory, they emit light in a wide spectrum in the same plane as the bending curve. Unfortunately the quality of the light beam in terms of focus and brilliance is not as good as that from an *Undulator*. Nevertheless, not all techniques requires a high brilliance and a collimated beam: EXAFS, for example, is perfectly suited for a *Bending Magnet* source.

The properties of the light generated from a synchrotron radiation source are definitely worth a mention:

High Brilliance: Brilliance is a quantity commonly used to evaluate the quality of a light beam. It considers the amount of photons within a particular solid angle, cross section and spectral area. It is defined as follows:

$$B = \frac{I_\gamma}{\Omega \sigma \Delta} \tag{2.4}$$

where I_γ is the number of incoming photons per second, Ω is the solid angle covered by the beam, σ is the beam cross section and Δ is the 0.1% width of the light spectrum. From an traditional X-Ray tube an increase of many orders of magnitude is possible, as shown in Figure 2.8.

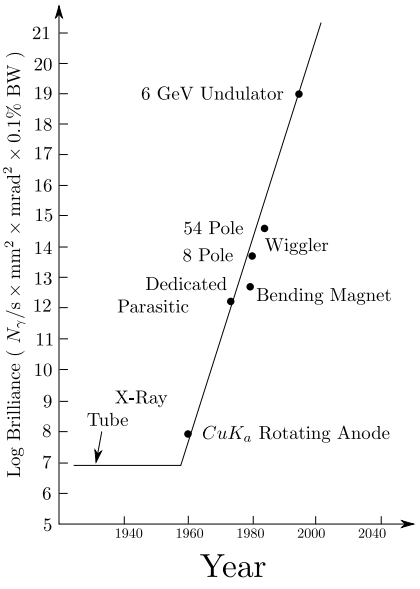

Figure 2.8: Evolution of brilliance in time

Low Divergence: As stated in the paragraph regarding the *Undulators*, the relativistic motion of the electron allows for the emission of an extremely collimated beam. Usually the divergence of the beam is in the order of 10 μrad (about $5 \cdot 10^{-4}$ deg).

Wide Spectrum and Tunability: The frequencies of the emitted light range from infrared to hard X-Rays. A particular energy can be either obtained by moving the magnets in a *Undulator* or with a monocromator. The origin of the wide spectrum is particularly clear when considering a *Bending Magnet*: the relativistic electron bent by the magnetic field irradiates the sample only for a tiny fraction of a second; this results in a very short pulse in time, which means a very broad spectrum.

Pulsed Light: Since the particles are accelerated in RF-synced cavities, this means that only particular bunches of electrons have the correct characteristics to survive in the booster and storage rings. Thus, the light is emitted in well separated (typically micro or nanoseconds) and narrow (even picoseconds) pulses. This is the basis for time resolved experiments.

Light Polarization: Polarization is a characteristic of huge interest for example in the study of magnetic materials, since the angular momentum of the photons may couple with the spin momentum of electrons. The light from a synchrotron is linearly polarized in the plane of the ring, but can also be made elliptic if the sample is moved above or below the plane (with the drawback of a lowering in intensity).

2.3 Beamline layout

2.3.1 General setup of a beam line

Typically, a beamline is composed of various optical elements aimed at focusing the X-Ray radiation on the sample. One of the first of these elements is a

monocromator: it is made of two reflecting crystals that, exploiting Bragg's law, are able to select a narrow range of energies from the incoming white beam. Bragg's law defines the angles of constructive and destructive interference when an X-Ray beam is reflected by the different atomic planes in a crystal. Given a spacing d between the planes, the condition for constructive interference is $2d\sin\theta = n\lambda$; as an example, when considering a cubic system, the distance between the planes can be expressed via the Miller indices in the following way

$$d = \frac{a}{\sqrt{h^2 + k^2 + l^2}} \tag{2.5}$$

giving the expression of the wavelength reflected at a chosen angle from a crystal cut along a particular axis:

$$\left(\frac{\lambda}{2a}\right)^2 = \frac{\sin^2\theta}{h^2 + k^2 + l^2} \tag{2.6}$$

Following up there are usually some mirrors used to precisely align the beam and reject higher harmonics that cannot be filtered with the monocromator. The mirrors are coated with different materials in order to have high reflectivity in a broad energy range. For example, Silicon can be used up to 10 keV, Palladium within 10-15 keV and Platinum from 15 to 20 keV. Mirrors are used instead of lenses due to the peculiar behaviour of light in the X-Ray regime. In this region of the spectrum the index of refraction for a material is typically slightly smaller than 1, allowing for a phenomenon called *total external reflection* when light rays are impinging with grazing incidence.

The beam then hits the sample and either the transmission or the fluorescence is measured.

2.3.2 The experimental hutch and the spectrometer

In a most common absorption experiment, a detector is placed after the sample to measure transmitted light; then the incident energy is scanned thanks to the monocromator and a full absorbance spectrum is recorded.

When performing a fluorescence measurement, two different setups are possible, both again exploiting the effects of Bragg's law [12].

In the *scanning spectrometer*, part of the fluorescent light is analysed and focused on the detector by spherically bent crystals placed on virtual circles which intersects at the sample and at the detector (see Figure 2.9). The position and angle of the crystals determines the position of the foci and the energy bandwidth. This is the instrumental setup used at ID26, where the data presented in the work were measured.

In the *dispersive spectrometer*, X-Rays with different energies hit at the same time a dispersive element, which diffracts them with different angles. The radiation is then focused on a position-sensitive detector that spatially resolves all the energies. This setup is more suitable for time-resolved experiments, as it allows, ideally, for the recording of a full spectrum in a single shot of X-Rays. Instead, it is not desirable for HERFD-XAS, as only a small fraction of the surface of the crystal reflects the desired fluorescent energy. Moreover, a scanning spectrometer is better suited for dilute systems, since the crystals cover a bigger solid angle and can pick up more radiation.

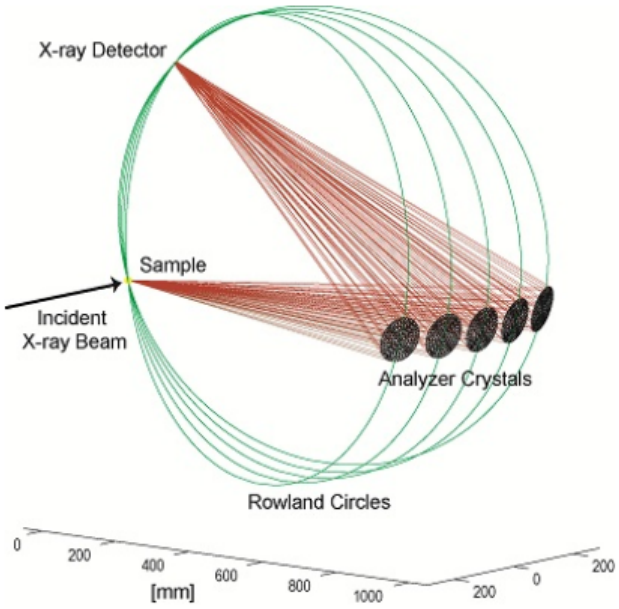

Figure 2.9: Setup of a scanning spectrometer.

Chapter 3

A Study of Irradiation Damage

The first part of this chapter is dedicated to the experimental data relative to the damaging process of BAM. All the measurements are done exploiting the HERFD-XAS technique (see Paragraph 2.1.3), which enables us to have an energy resolution in the order of the eV ($\frac{\Delta E}{E} < 0.001$).

In Sections 3.3 and 3.4, a statistical analysis is presented and applied with the aim of discovering the factors that are responsible for BAM:Eu degradation. This will lay some basis upon which the simulations in Chapter 4 will be interpreted.

3.1 Sample Preparation

In X-Ray spectroscopy the preparation of the sample can be fairly easy, as, if the sample is in powder form, it can be simply compressed in a pellet. This is what was done to prepare the samples used in the experiments, the composition of which is listed in Table 3.1. Regarding the material under study, six samples were available, considering both the un-doped and doped crystal: BAM, BAM:Mn, BAM: Eu and BAM: Eu, Mn (the latter two in double copy from different manufacturers). The references were chosen depending on the availability of the materials and the similarity in the oxidation states of Europium or Barium.

Unfortunately, among the samples from Philips, an un-doped sample is not available and, since the production process from this manufacturer is patented, it is unknown how the doping was obtained. This does not allow us to know if the single and co-doped BAM powders were obtained with different procedures.

The damaging of the sample was achieved either via X-Ray irradiation or via annealing at 1000 degrees. The irradiation has taken place between different XANES measurements (each measure lasting about 4 seconds) and in different points on the sample with an exposure time ranging from 5 to 1300 seconds; annealing has been carried out in air.

Table 3.1: Samples considered in the present work

Name	Doping	Manufacturer	Particle size
BAM	un-doped	Gent Lumilab	n/a
BAM:Mn	6 %	Gent Lumilab	1 μm
BAM:Eu	6 %	Gent Lumilab	1 μm
BAM:Eu	7 %	Philips	5 μm
BAM:Eu,Mn	3 % and 6 %	Gent Lumilab	1 μm
BAM:Eu,Mn	15% and 31%	Philips	5-10 μm

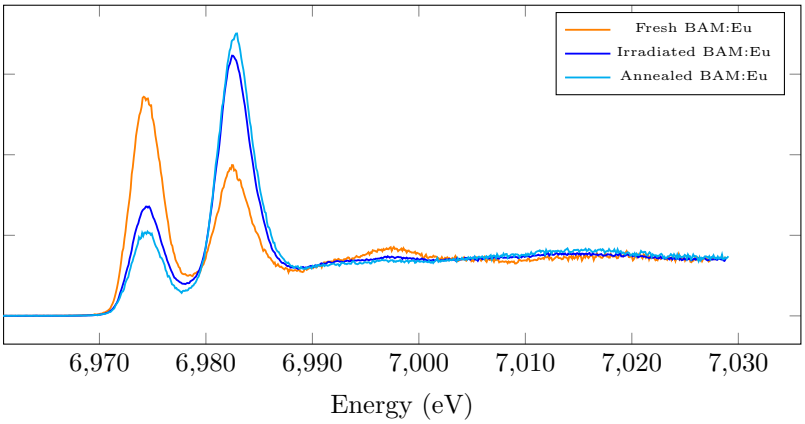

Figure 3.1: Initial and final condition for the Eu when studied at the L_{III} edge

3.2 Effects of Irradiation and Annealing

The effects of the damaging process have been recorded trough a series of XANES spectra on Europium and Barium. The X-Ray beam has been used both to probe the local structure around the absorber and to obtain the desired degree of damage.

For the Europium, a series of 12 XANES spectra has been recorded in order to study the dependence on the exposure to X-Ray irradiation. The whole set of results can be seen in Figure 3.3 on page 24, while the initial and final situation are highlighted in Figure 3.1 (where also the annealed BAM:Eu is shown).

As common practice is to correlate the position of the white line with the oxidation state, a first interpretation is the gradual shift from Eu^{2+} to Eu^{3+}. Other causes that could explain this behaviour have been presented in Section 1.3, but are harder to put in perspective when looking at the measurements. Considering the Europium physical shift, for example, two different positions in the unit cell could give rise to the two peaks and a shift from one site to the other would also gradually redistribute the intensity.

The analysis in the second part of this Chapter will be focused exactly on this dataset and, together with first-principle calculations, will be aimed at understanding if the shift in intensity is due to oxidation or to a physical change in the crystalline structure.

Already by looking at Figure 3.1, it is possible to suppose that the effects

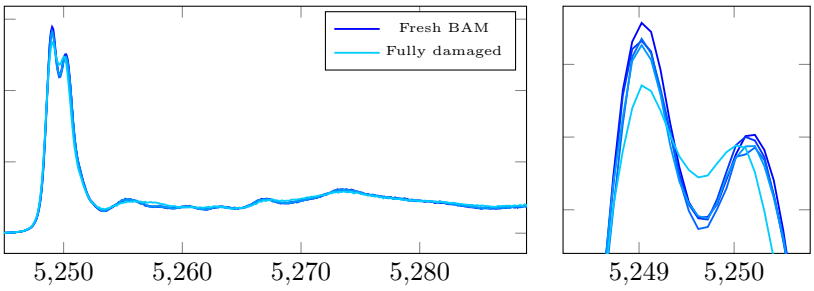

Figure 3.2: Ba L edge with BAM exposed to X-Ray radiation. Intermediate steps were taken after 20, 40 and 60 minutes, while the fully damaged BAM corresponds to 3.5 hours of irradiation.

of annealing and irradiation are similar and in Section 3.4.2, a procedure to quantitatively evaluate this idea will be presented.

For Barium, the conducted experiment is similar to the one done for Europium with a varying exposure time to irradiation; the results (see Figure 3.2) do not show huge variations, if not in the double-peaked white-line.

More extensive changes would be expected in these last spectra if the Europium were to move around: the different sites cited in literature for the dopant atom are all near Barium and a non-negligible occupancy would be readily detected by a XANES measurement, as this technique is sensitive to the local structure around the absorber.

This is a first suggestion that, as the underlying physical phenomenon, oxidation is the favourite: in contrast to a change in position, a difference in the valence state of Europium would not have such a great impact on a Barium atom at 5 or more angstrom away.

The damaging has no effect on the Manganese K edge and this confirms the well-established idea in literature that the spinel block is not as sensitive as the mirror layer. Carrying little useful information to the present discussion, Manganese XANES and v.t.c. XES will be better described in the following chapter, together with their relative simulations.

3.3 Theory of PCA and FA

In order to better understand the underlying factors in the damaging process in BAM:Eu, a statistical tool has been used. The theory (current section) and the application (section 3.4) are both presented, giving some details on the required hypotheses and the exploited algorithms.

The overall idea is to calculate the number of components that can influence the variation in the intensity of the spectra. This could help in understanding if the damaging is due to oxidation (two components would be present, one for Eu^{2+} and one for Eu^{3+}) or to a change in the crystal structure (there could up to a component for each crystallographic site). It is important to stress that this technique is purely statistical: the physical interpretation of the results comes

in a second time (for example thanks to comparison with calculations, as done in the next Chapter).

3.3.1 Principal Component Analysis

Principal Component Analysis (PCA) is a multivariate technique which was introduced and developed by Person [34] and Hotelling [20]. In the past years it has been applied to the analysis of EXAFS and XANES spectra [11, 37, 22] and used together with factor analysis and a procedure called target transformation. PCA can be used as a descriptive technique in order to better understand the behaviour of hidden variables in a dataset. In particular the main advantage is the dimensionality reduction: the whole set can be expressed (given some approximation) in function of a reduced number of variables.

The theoretical derivation is carried out in [24, 31] and in a more naïve way in [40]. It will be shown again here keeping in mind that in this case the data represent X-ray absorption spectra.

Considering the original data expressed as an $m \times n$ matrix M, all the measurements can be pictured in a n-dimensional vector space spanned by an appropriate orthonormal basis. The spectra can be represented either as rows or as columns, the final result will not change; in this work the former choice is made. Thus m is the number of measurements and n is the number of data points in each spectrum. The aim is to find a different orthonormal basis in which to re-express all the m vectors, considering the constrain that the process should maximise the variance for each of them and minimize the covariance between every couple.

The origin of this objective lays in the assumption of PCA that all relevant information in the dataset is hidden in the variability of the vectors. The new basis is able to order the transformed vectors depending on their variance and thus tells us which of them are more important for an accurate representation of the original dataset.

Mathematically, the variance of a vector is obtained via the norm and the covariance via the dot product (we suppose that each vector has average 0). Considering the matrix formalism we are using, we can define an $m \times m$ matrix C such that $\mathrm{C} = \frac{1}{n-1}\mathrm{M}\mathrm{M}^T$: in this way the element $\{i, j\}$ represents the covariance between the i^{th} and j^{th} vector. When $i = j$ the result is the variance.

In this picture the solution to the problem is achieved via the diagonalization of the covariance matrix C which results in

$$\mathrm{C} = \mathrm{P}\Lambda\mathrm{P}^{-1} \tag{3.1}$$

In this case P will be the matrix of *principal components* (they coincide with the eigenvectors) and Λ will contain the relative eigenvalues λ_i on the diagonal. P is an orthonormal matrix and defines a new set of axis which accounts for the variance of the dataset depending on the magnitude of the relative eigenvalues. This means that once the eigenvectors are ordered with respect to their eigenvalues, it is possible to use only the first of them to account for the variation of the whole set.

It is then possible to project the original data matrix in the new space obtaining

$$\underset{m\times n}{\mathrm{O}} = \underset{m\times m}{\mathrm{P}^T}\ \underset{m\times n}{\mathrm{M}} \tag{3.2}$$

It is important to note that, in general, neither the principal components matrix P nor the projected matrix O carry an intrinsic physical meaning. Only in some particular cases it is possible to give an interpretation; some examples are given in chapter 4 of *Principal Component Analysis* [24].

Once the projection and the principal component are obtained, a subspace of this dataset can be chosen as the one containing the relevant information. This subspace is defined by the most important components, that is, those from which the matrix M can be rebuilt with maximum accuracy. Supposing that the number of principal components is s, then the first s column will be chosen from P and the first s rows will be chosen from O obtaining the reduced $m \times s$ and $s \times n$ matrix $\tilde{\mathrm{P}}$ and $\tilde{\mathrm{O}}$. From those the reconstruction equation is simply

$$\underset{m\times n}{\tilde{\mathrm{M}}} = \underset{m\times s}{\tilde{\mathrm{P}}}\ \underset{s\times n}{\tilde{\mathrm{O}}} \tag{3.3}$$

If the correct number of component is chosen then the discrepancy between M and $\tilde{\mathrm{M}}$ will be below the experimental error.

An alternative way to deduce the principal components is to use the *singular value decomposition*. This algorithm consists in the decomposition $\mathrm{X} = \mathrm{USV}^T$ where U and S contain respectively the eigenvectors and eigenvalues of XX^T. Thus, considering $\mathrm{X} = \frac{1}{\sqrt{n-1}}\mathrm{M}$, we have the identities U = P and $\mathrm{diag}(\Lambda) = \mathrm{diag}(\mathrm{S})$.

Choosing the correct number of principal components is not always straightforward. Malinowski [31] and Jolliffe [24] give some insight on the criteria upon which the choice should be made. As said before, the magnitude of the eigenvalues λ_i can be used to address the importance of each component, but still, considering a number big or small is much subjective. Two quantitative functions can be used in this context:

$$IE(i) = \sqrt{\frac{i\sum_{j=i+1}^{n}\lambda_j}{mn(n-i)}} \qquad IND(i) = \sqrt{\frac{\sum_{j=i+1}^{n}\lambda_j}{m(n-i)^5}} \tag{3.4}$$

The minimum of IE and IND as a function of i corresponds to the number of principal components to take into account. The reason is that these two functions evaluate the error in the reconstruction of the original data with respect to the number of components used. The error is high when the number of components is too small (there is not enough information) or too big (only redundant information or noise is added).

3.3.2 Factor Analysis

Here a brief summary of Factor Analysis is given following the explanation by Malinowski [31]. FA is a multivariate technique in which an underlining linear relation between the hidden variable is known to exist (this is the difference with PCA, in which no likewise assumption was made). Thus the data matrix can be expressed in the same form as before M = PO, but now with the added information that among all possible couples of P and O, there is one in which the two matrix have a precise physical meaning. In this particular case O would be containing s pure spectra which are linearly combined via the coefficients in P to give the dataset.

Again, finding the matrices of interest is not easy. In particular we can consider any invertible matrix R and apply the transformation

$$\mathrm{M} = \mathrm{PRR}^{-1}\mathrm{O} \tag{3.5}$$
$$= \mathrm{P}'\mathrm{O}' \tag{3.6}$$

where P' and O' still satisfy the equation but lose any physical meaning. Thus we should keep in mind that this problem has not a unique solution. One of the two following methods can be exploited (depending whether information about the pure spectra is available or not) in order to extract the physical solution from the whole range of mathematical solutions.

Target Transformation

In this case, as explained in previous papers [31, 43, 19], the matrix O and the eigenvalues of C can be used to test if a reference pure spectra is present in the linear combination that gives the columns of the data matrix M. Doing this procedure multiple times allows to build a set of vectors that would be suitable candidates for the matrix O.

Starting from a reference spectra $\mathbf{x}$, the equation

$$\tilde{\mathbf{x}} = \mathrm{O}^T \Lambda \mathrm{O}\, \mathbf{x} \tag{3.7}$$

provides a new vector $\tilde{\mathbf{x}}$ that has to be compared with $\mathbf{x}$; if the difference is below the experimental error, then the suspected vector is part of the linear combination. Equation 3.7 is obtained from a least square fit between $\mathbf{x}$ and an unknown vector whose components are weighted by the elements of O. The matrix used is O because it is also the one that connects the principal components to the data matrix.

Once a set of spectra $\{\mathbf{x_i}\}$ has been chosen following the above-mentioned procedure, then the matrix

$$\mathrm{Z} = \left[\, \mathbf{z_1}\, \mathbf{z_2} \ldots \mathbf{z_s} \,\right] \quad \text{where} \quad \mathbf{z_i} = (\tilde{\mathrm{O}}\tilde{\mathrm{O}}^T)^{-1}\tilde{\mathrm{O}}\mathbf{x_i} \tag{3.8}$$

can be used to obtain the coefficients in the relation

$$\mathrm{M} = \mathrm{YX}^T \tag{3.9}$$

where $\mathrm{X} = \left[\, \mathbf{x_1}\, \mathbf{x_2} \ldots \mathbf{x_s} \,\right]$ and $Y = \tilde{\mathrm{P}}(\mathrm{Z}^{-1})^T$.

Thus a matrix X with physically meaningful columns (the pure spectra) is obtained and also the coefficient matrix Y is given. If some reference data is available, this is the best way to proceed, otherwise the method shown in following paragraph provides a good alternative with some drawbacks.

Non-Negative Matrix Factorization

A different way to obtain the two matrices X^T and Y is the *non-negative matrix factorization*. In this kind of decomposition the data matrix is separated in two contributions as $\mathrm{M} = \mathrm{AS}$ (S is not related to the singular values cited before) with the constrain that $\mathrm{A} \geq 0$ and $\mathrm{S} \geq 0$. An iterative algorithm to obtain the matrices can be found in Lee and Seung [29] and can be further expanded in

Table 3.2: Values obtained from the PCA algorithm with respect to the number of components i

i	1	2	3	4	5	6
Variance	3.3668	0.0494	0.0006			
Explained Variance (%)	98.51	1.446	0.0189			
$IE\,(\times 10^4)$	228	57	56	63	69	75
$IND\,(\times 10^4)$	7	1	1	2	2	3

order to account for the normalization of the spectra [10, 17]. The multiplicative rules used are

$$\mathrm{S}_{ij} \leftarrow \mathrm{S}_{ij}\frac{(\mathrm{A}^T\mathrm{M})_{ij}}{(\mathrm{A}^T\mathrm{AS})_{ij}} \qquad \mathrm{A}_{ij} \leftarrow \mathrm{A}_{ij}\frac{(\mathrm{MS}^T)_{ij}}{(\mathrm{ASS}^T)_{ij}} \tag{3.10}$$

where A and S are inizialized as matrices of random numbers. These multiplication rule have been obtained considering a cost function based on the 2-norm of the matrices:

$$\left\| \mathrm{M} - \mathrm{AS} \right\|^2 = \sum_{ij} (\mathrm{M}_{ij} - (\mathrm{AS})_{ij})^2 \tag{3.11}$$

Not being a closed-form problem, not even in this case there is the certainty of getting the right physical solution. Nevertheless, given the number and kind of constrains it is reasonable to expect a matrix S not far from the real pure spectra.

3.4 Application of PCA to Eu XANES spectra

All the previous algorithms have been applied to the 12 Eu XANES (see Figure 3.3) in order to understand how many components were present and, eventually, to obtain the pure spectra that could originate them in a linear combination. This set of measurements is the one obtained by an increasing exposure to X-Ray irradiation, a damage that would simulate lifetime effects in a plasma display panel.

3.4.1 Application of PC analysis

The measurements have been placed in a matrix in which each row corresponds to a spectra. Then PCA was applied using both the *svd* algorithm and the diagonalization algorithm: the results between the two were identical.

After applying the PCA, the values shown in Table 3.2 have been obtained. The conclusion is that there are two main components, although the IE and IND minima could be also seen to lie at $i = 3$ (i being the number of components). This hypothesis is confirmed by the reconstruction shown in Figure 3.4: already considering two components allows for a good reconstruction of the spectrum, meaning that all the other do not contribute with significant information.

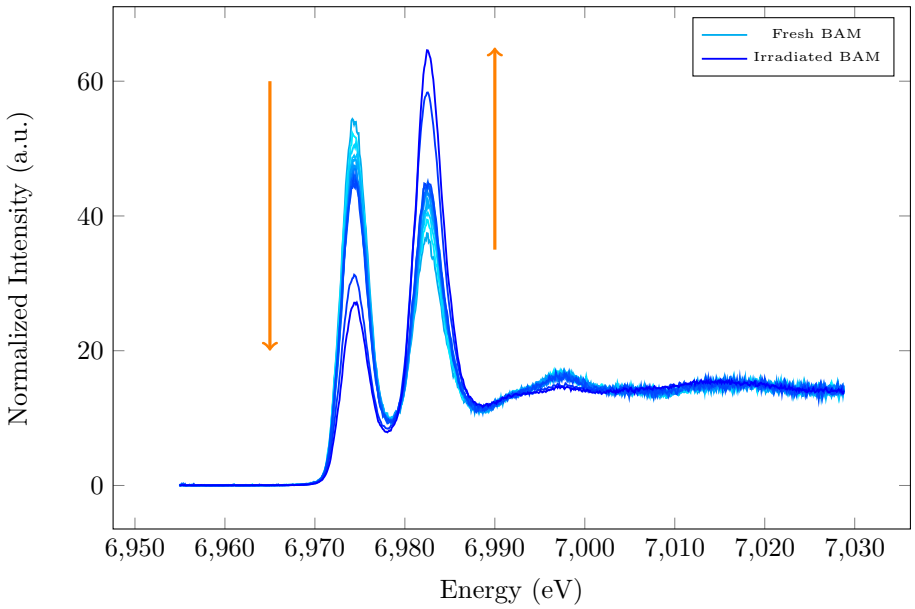

Figure 3.3: The twelve normalized XANES spectra used for the analysis. The damaging process is graphically shown as a shift in color.

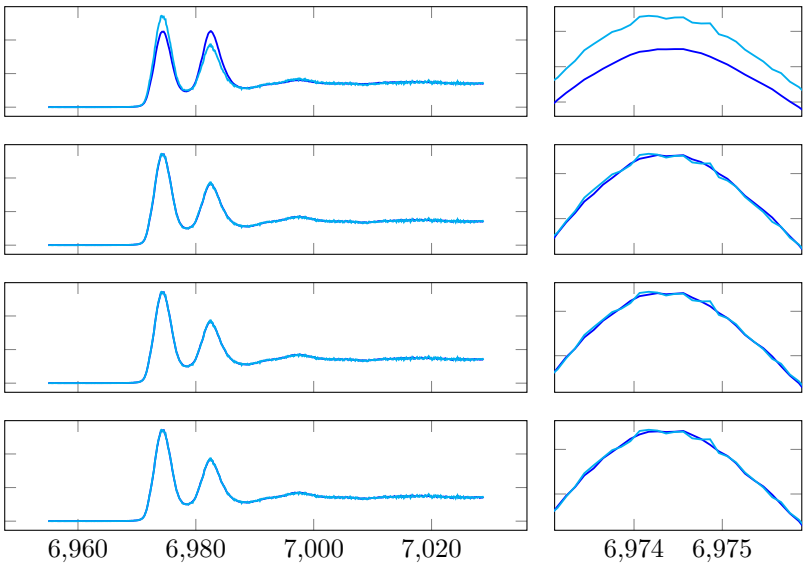

Figure 3.4: The first of the twelve spectra is shown reconstructed using 1,2,3 and 4 components (from top to bottom). In the inset the low-energy peak is shown.

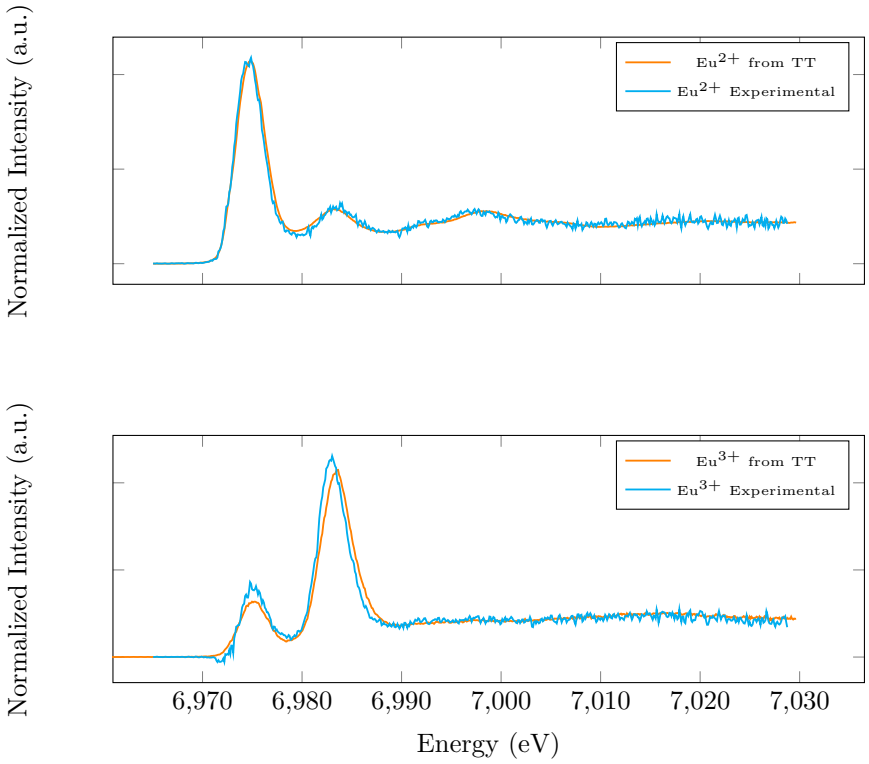

Figure 3.5: Top: Candidate and transformed spectra for a sample with high concentration of Eu^{2+}. Bottom: Candidate and transformed spectra for a sample with high concentration of Eu^{3+} obtained with annealing at 1000 degrees C.

3.4.2 Application of Target Transformation

This transformation has been applied to a couple of spectra (taken in different experimental conditions) which were supposed to probe two samples containing the pure elements present in the mixtures. These two candidates were a fresh BAM:Eu sample and an annealed one (according to literature, annealing in air should be a reliable way to oxidise Europium). This will give us a way to understand if effects from irradiation and annealing are compatible with each other.

As seen in Figure 3.5 the reconstruction is quite good and hints that the two reference spectra could really be in the linear combination. A slight shift is observed in one of the transformations: this is due to the fact that the annealed BAM:Eu sample shows itself a small deviation with respect to the irradiated sample. Since the TT algorithm carries information on the 12 spectra, this shift is in turn found in the output. The coefficients that, once applied to the pure spectra, generate all the 12 combinations are shown in table 3.3 and compared with the results from the Non-negative Matrix Factorization in Figure 3.8.

As it has already been shown in Figure 3.1, the spectra from the annealed and irradiated sample were not very different to start with. This Target Trans-

Table 3.3: Each row of the table shows an estimated amount of the Eu^{2+} or Eu^{3+} pure spectra in the n^{th} spectrum of the data series. This values are plotted in Figure 3.8

Spectrum number	From TT		From NNMF	
	Eu^{2+}	Eu^{3+}	Eu^{2+}	Eu^{3+}
1	0.6718	0.3416	0.7917	0.2835
2	0.6257	0.387	0.7451	0.3251
3	0.5946	0.4187	0.7138	0.3542
4	0.5702	0.443	0.6894	0.3764
5	0.553	0.4607	0.6721	0.3924
6	0.5324	0.4798	0.651	0.4103
7	0.5202	0.4924	0.6387	0.4219
8	0.5072	0.5056	0.6258	0.4338
9	0.4966	0.5167	0.615	0.4441
10	0.488	0.5245	0.6062	0.4513
11	0.2111	0.8011	0.3268	0.7053
12	0.1129	0.9054	0.2285	0.8008

formation has in some way only confirmed what was already apparent from a quick glance at the measurements.

3.4.3 Application of NNMF

The algorithm from Equations (3.10) has been implemented in MATLAB with the constrain of normalization. After 2000 iterations and supposing only two components, the spectra shown in Figure 3.6 have been obtained. The qualitative behavior of the function is correct although there are some differences in the magnitude and position of the peaks.

The results obtained with the NNMF algorithm considering 3 components are shown in Figure 3.7. Two different results are shown in order to understand that very different solutions can be obtained from one run to another. Given that the cost function in Equation 3.11 has more than one minima, it is not granted that the same solution is found after every calculation nor it is necessary that convergence is reached in the same number of iterations. Beside the input matrix, the only other parameter in the algorithm is the convergence threshold; this can be either a chosen number of iterations or the difference between the output of two consecutive cycles.

Using three components rather than two does not add any particular additional information. The third spectrum (the orange one in Figure 3.7) seems to be only an intermediate step between the initial and final configuration, its existence being justified only by the explicit request of three components.

The coefficients for the linear combination obtained from the algorithm are written in the last two columns of table 3.3 and plotted in Figure 3.8.

3.4.4 Conclusions from the analysis

In conclusion to the analysis, it appears that there are either two or three components determining the shift in intensity among the 12 spectra. Even if

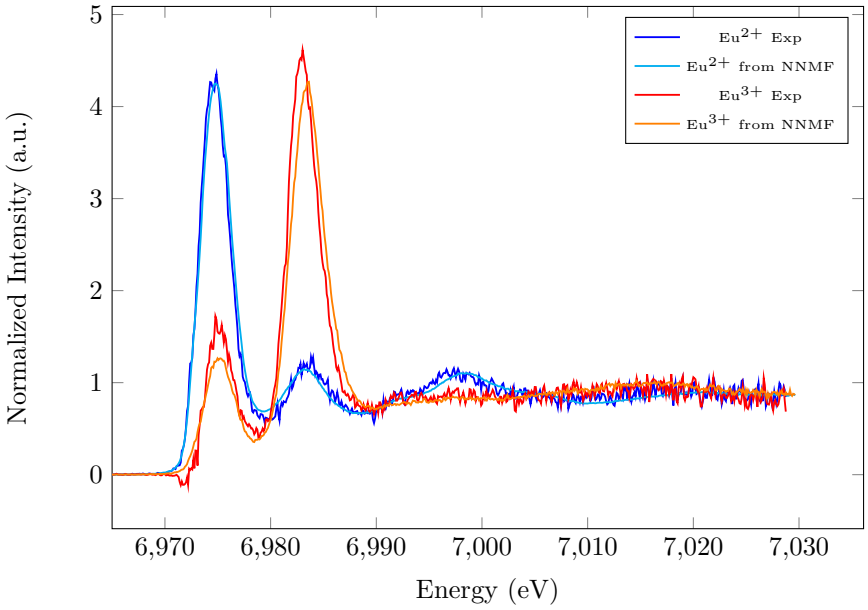

Figure 3.6: Four spectra are shown: the two experimental references and the two obtained from NNMF.

the IE and IND could point toward the presence of a fourth component, the spectra are represented to a very good precision already with 2 or 3 factors.

It is also very interesting to note that an algorithm like the NNMF is able to extract valuable information without any input parameter beside an expected number of components. This number can be the outcome of a Principal Component Analysis, but could also be an educated guess.

Given what was expected at the beginning of this section, the number of factors point towards the oxidation as the main cause behind the change in intensity. On the other hand, this analysis is not able to discriminate the possibility that only two crystallographic sites are taking part in the damaging process. If this is the case (for example, only BR and aBR sites are present in the crystal), then two components would be expected as well.

Unfortunately, assigning PCA-detected components to physical phenomena is not obvious and is beyond the scope of this particular kind of analysis. What can be said, thanks to the Target Transformation, is that the effects induced by the irradiation are compatible with those from the annealing: the spectrum obtained from the annealed BAM is considered as a plausible element of the linear combination that generates the 12 spectra.

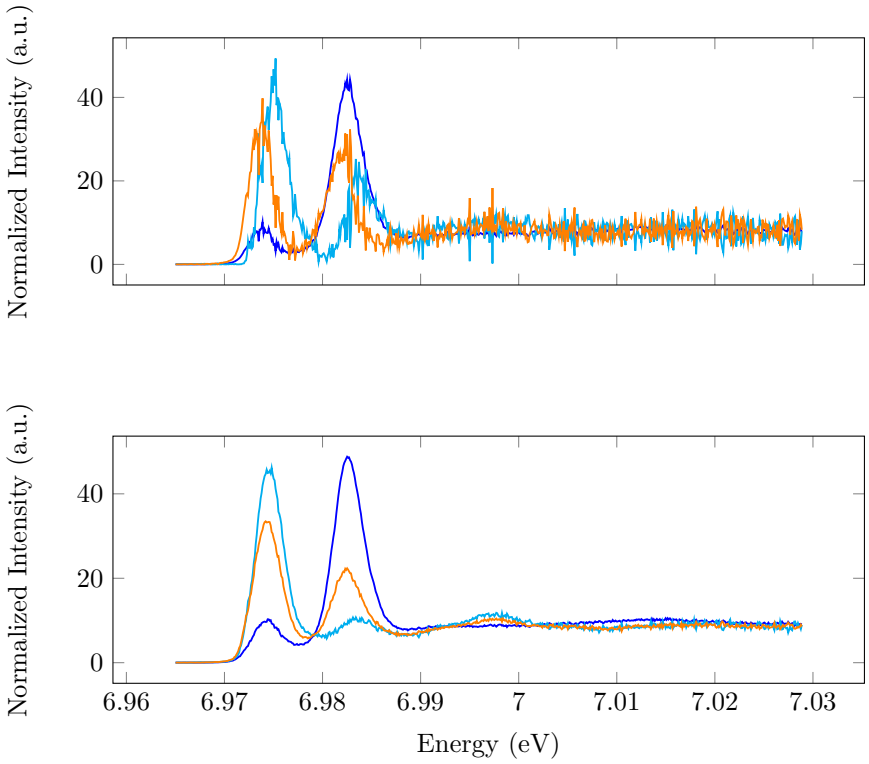

Figure 3.7: Different run of the NNMF algorithm as seen after 2000 iterations. Here three components have been considered just to see if the third could represent something meaningful.

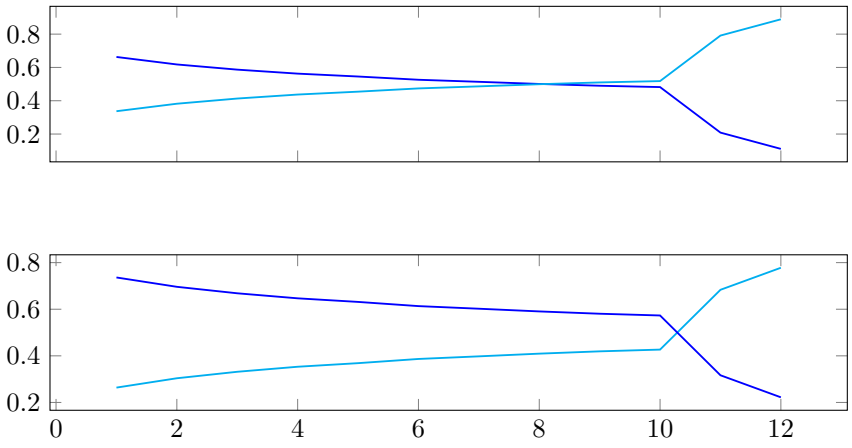

Figure 3.8: Top: Coefficients obtained from the TT method for the twelve spectra. Bottom: Coefficients obtained from the NNMF. The numbers are tabulated in Table 3.3

Chapter 4

Simulations of Spectral Properties

4.1 Software description

This section will be divided between the description of the two software used for the simulations (`FEFF9` and `fdmnes`) and the results obtained from them. Both codes were run on the ESRF computing cluster, exploiting parallelization features where available. The main difference among the two is in the mathematical procedure used to solve the problem of computing a spectrum: both are DFT codes but `FEFF9` uses the muffin-tin approximation for the potential while `fdmnes` can keep its shape free with the drawback of a slower calculation. More details are given in the two following sections.

There is one issue worth mentioning when doing simulations for HERFD-XAS measurements. As stated in Section 2.1.3, this technique relies on the fact that in the X-Ray energy range the radiative decay (detected by the spectrometer) and the absorption coefficient have the same behaviour. Simulation software like `FEFF9` and `fdmnes` are not made to account for the whole second-order process of absorption and emission: instead, they are meant for more common absorption measurements.

The biggest limitation is that secondary processes cannot be described in the framework of one-electron theories [7] and `FEFF9` , despite not being a strictly one-electron code, provides only an approximate approach to multi-electronic interactions. In this context `fdmnes` should offer more reliable results as in the last update some support for this kind of calculations has been added.

It seems, though, that often a simple reduction of the core hole lifetime is sufficient to obtain satisfactory results from `FEFF9` [42] and possible discrepancies should be limited to low energies and the pre-edge, where electron-electron interactions are significant [15].

4.1.1 FEFF and the Green's Function Formalism

`FEFF9` is a commercially available software developed at the University of Washington used for calculating excitation spectra and electronic structures. Among the spectroscopic properties that can be calculated (and that are of interest in the present work) there are extended X-Ray absorption fine structure (EXAFS),

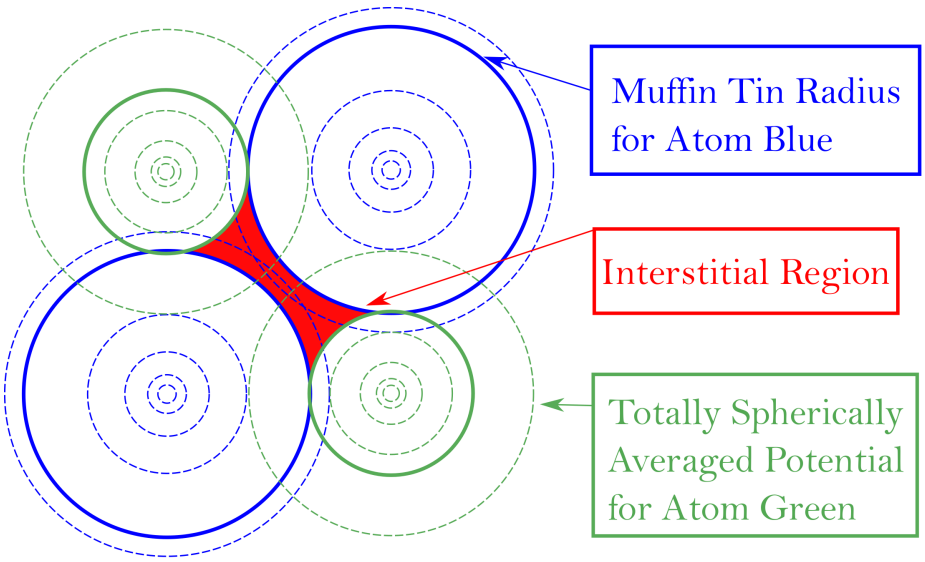

Figure 4.1: Schematic drawing of the muffin-tin potential: dotted lines are contour lines for the potential, while the bold circle is extent to which the potential is non-constant.

X-Ray absorption near edge structure (XANES) and X-Ray emission (XES).

The code is based on self consistent calculations and multiple scattering events (as a way to describe the path of the electron) in a spherically symmetric muffin-tin potential. The simulation is performed through multiple steps: (1) obtaining the potentials, (2) finding the scattering amplitude and (3) solving for the XAS/XES spectrum.

In the first step, initially, a free atom is considered for each atomic species and the relative potential V_i is calculated with a Dirac-Fock DFT code; then the scattering potential (that is, the one that will be used in step (2)) is obtained by overlapping all the different V_i in a muffin-tin approximation. This is known as the *Mattheiss prescription* and treats the atoms as "hard" spheres of potential packed together in a lattice where the interstitial region between the nuclei presents a constant potential (see Figure 4.1). Despite the strong approximation, this approach gives surprisingly good results.

Then, (in step (2)) the projected density of states and the Green's function are calculated. For the second task two methods are available [36], one being more suitable for near edge spectroscopies (XANES), and one for energies high above the edge (EXAFS). These two methods are the Full Multiple Scattering and the Path Expansion.

To explain the difference among the two and to explain what is the use of a Green's function in this context, a little digression is needed. In order to evaluate the absorption coefficient one has to calculate the total absorption cross-section using Fermi's golden rule. On the other hand, the use of the golden rule requires to know the final states of the transition and their calculation is computationally expensive: it is more efficient to re-express the equation for the XAS intensity in terms of a photoelectron Green's function propagator G which implicitly sums over all final states[6].

The exact form of G is the following

$$G(E) = \sum_f |f\rangle \frac{1}{E - E_f + i\Gamma} \langle f| \tag{4.1}$$

where the summation is taken over all final states and Γ is the core hole life time. In this formalism the contribution to the cross section from an initial state $|i\rangle$ becomes

$$\sigma(E) = 4\pi \frac{\omega}{c} \sum_{L,L'} M^*_{L,i}(E) \rho_{L,L'}(E) M_{L',i}(E) \tag{4.2}$$

where $M_{L,i}$ is the dipole matrix element between the core state and a scattering state $|L\rangle$. $\rho_{L,L'} = \frac{1}{\pi}\mathrm{Im}[G_{L,L'}]$ is an element of the spectral density matrix, which can be split in two parts as G separates in a contribution from the central absorbing atom G^c and one from the environment G^{sc}. The first defines the first order atomic background μ_0 (defined by the potential on the atom) and the second the fine structure χ (given by the multiple scattering from the surroundings).

The correct form of the matrix element $G^{sc}_{L,L'}$ would be

$$G^{sc}_{L,L'} = [(1 - G^0 T)^{-1} G^0]_{L,L'} \tag{4.3}$$

where G^0 is the free electron propagator (it describes the path of the photoelectron between two points along the interstitial region) and T is the atomic scattering matrix (which describes the bouncing off from an atom).

The inversion of the matrix $(1 - G^0 T)$ in this last equation is often difficult, and thus an approximated expansion, the Path Expansion, is used:

$$G^{sc}_{L,L'} = [G^0 T G^0 + G^0 T G^0 T G^0 + ...]_{L,L'} \tag{4.4}$$

where the terms represents single, double and higher order scattering. Thus G considers all possible ways in which a photoelectron can scatter before the core hole is filled again.

Now the two methods that were mentioned before this digression can be better understood. For high energies (for example in EXAFS) the Path Expansion converges rapidly and thus can be efficiently used in calculations. In other contexts (for example in XANES) this is not a viable option, and the whole matrix must be explicitly inverted: this is the Full Multiple Scattering method.

Finally, going back to how the software works (and this is step (3)), after the computation of the Green's function, `FEFF9` can calculate the spectrum $\chi(k)$ or $\mu(E)$ and save it to a file.

Input File

The software reads the instructions to perform the calculation from a plain text file. In this file are specified the crystal structure and a number of keywords with additional information. Some of these keywords are presented here in order to show the basic parameters considered in the calculations for the current work.

`EXCHANGE` This card specifies which kind of exchange potential to use in the DFT calculation and the entity of its real and imaginary part. The potential used is the Hedin-Lundqvist, while the imaginary part is taken to be negative in order to reduce the core hole lifetime.

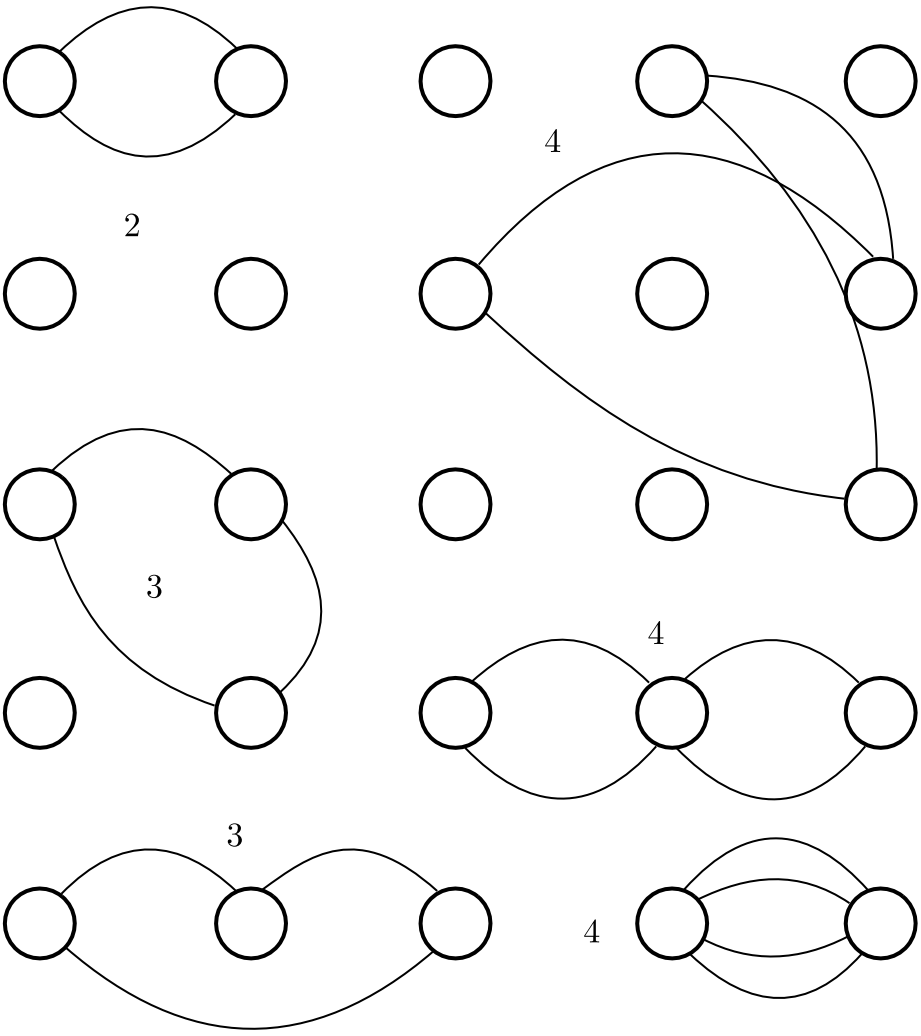

Figure 4.2: Here different order scattering path are shown. Each of these corresponds either to a term in the sum in Eq 4.4 or is implicitly considered in Eq 4.3. The Figure is from Ravel [35].

`SCF` The Self-Consistent-Field calculation is performed on a 4-5 Å cluster of atoms.

`FMS` The Full-Multiple-Scattering calculation is done on a bigger cluster: from 6 to 9 Å.

`COREHOLE` This specifies how to treat the core-hole left by the incoming photon. The Final-State-Rule is used, meaning that the dynamics of the excitation process are neglected.

`ION` **and** `CONFIG` These two cards are used to set a net charge on each atomic species. They have no effect when a SCF calculation is performed: the software converges to the same solution regardless of the initial configuration.

`ATOMS` **and** `POTENTIALS` These cards are used to specify the structural position and the atomic species present in the calculation.

4.1.2 fdmnes and the finite difference method

`fdmnes` [25, 5] is a code developed at Insitut Neel in Grenoble that also aims at simulating X-Ray spectroscopies and calculating cross-sections in the energy range of XANES and EXAFS. The main difference with `FEFF9` lies in the use of the Finite Difference Method (FDM): this allows for an unrestrained potential shape (contrary to the muffin-tin approximation) and should yield more reliable results.

As already stated, in the evaluation of the photo-absorption cross-section

$$\sigma \propto \sum_{f,i} |M_{if}|^2 \delta(\hbar\omega - E_f + E_i) \tag{4.5}$$

the difficulty resides in calculating the final states $|f\rangle$, as the initial state $|i\rangle$ is an atomic core orbital and the matrix elements M_{if} can be easily accounted for within dipole or quadrupole approximation. This cumbersome task was avoided with `FEFF9` thanks to the Green's function formalism (Eq. 4.1 and 4.2) but here is carried out with the FDM.

The FDM is a general procedure to solve differential equations and is based on the discretization of the volume where the calculation is to be performed. In this case we want to solve the Schröedinger equation on a spherical cluster of atoms centered on the X-Ray absorber. The unknowns are the amplitudes of the wave function in every grid point $\vec{\mathbf{r}}_i$: $\psi_i = \psi(\vec{\mathbf{r}}_i)$ and by discretizing also the potential $V_i = V(\vec{\mathbf{r}}_i)$ one obtains, for every grid node, an equation that depends also on the neighbouring points. The meshing of the volume needs not be homogeneous and the solutions in different regions (e.g., within and outside the cluster) are connected with adequate boundary conditions.

Before starting to solve the set of equations, the potential has to be found. This is done with DFT methods with the Local Density Approximation and considering the Hedind-Lundqvist exchange-correlation potential. In this way the only approximation the potential encounters is the discretization on the grid.

The problem is then cast in matrix form and solved as a linear system of equations; the final states are thus obtained and this allows for the evaluation of the cross-section in Eq. 4.5.

Input File

This second software works in a very similar way to `FEFF9` : a text file containing specific keywords is used to give instruction to the code. Among the keywords used are the following:

`SCF` Performs a Self-Consistent-Calculation

`GREEN` Optional - If present, performs a calculation with the Green formalism (like `FEFF9`) instead of the Finite-Difference-Method.

`RADIUS` Radius of the cluster where final state calculation is performed. A value between 6 and 8 Å is used.

`ATOM` Allows to explicitly set the electron configuration on each atomic species. Not necessary if the calculation is self-consistent.

`MOLECULE` **or** `CRYSTAL` Define the atomic positions either as a cluster of atoms or as a unit cell.

`CONVOLUTION` Specifies the width of the convolving function (between 0.2 eV and 0.5 eV for the current calculations).

4.2 Discussion of results

In the current section all the results from the first-principle calculations will be presented. Firstly, some comparisons with reference samples will be carried out in order to assess the reliability of the two software. Secondly, BAM simulations will be shown as a tool to infer some considerations on the crystal structure and the oxidation state of the atoms.

The simulations for BAM from `fdmnes` are concentrated in a dedicated section, as the differences between the results required an analysis by themselves.

4.2.1 Simulation of reference spectra

Many reference materials have been considered, the choice being made upon the availability of experimental data and simplicity of their crystal structure.

For Barium, the Barium Sulphide (BaS) has been considered. It crystallizes in the NaCl structure with Ba^{2+} and S^{2-} in octahedral sites: the well defined ionization numbers make it a good candidate to test the charge transfer evaluation of `FEFF9` .

For Europium, three different compounds have been examined: EuS, EuF_3 and Eu_2O_3. The most important difference among the three is the oxidation state of Europium: in the first there is Eu^{2+} while in the other two there is Eu^{3+}.

The most important common characteristic among the four comparisons (shown in Figure 4.3) is the fact that often the features beyond the white-line are well identified, although their energy position relative to the edge is not correct. This is what is highlighted mostly by BaS (top left plot): three features are correctly found but their position is too near the edge. They would most probably correspond to the experimental peaks identified by the orange arrows.

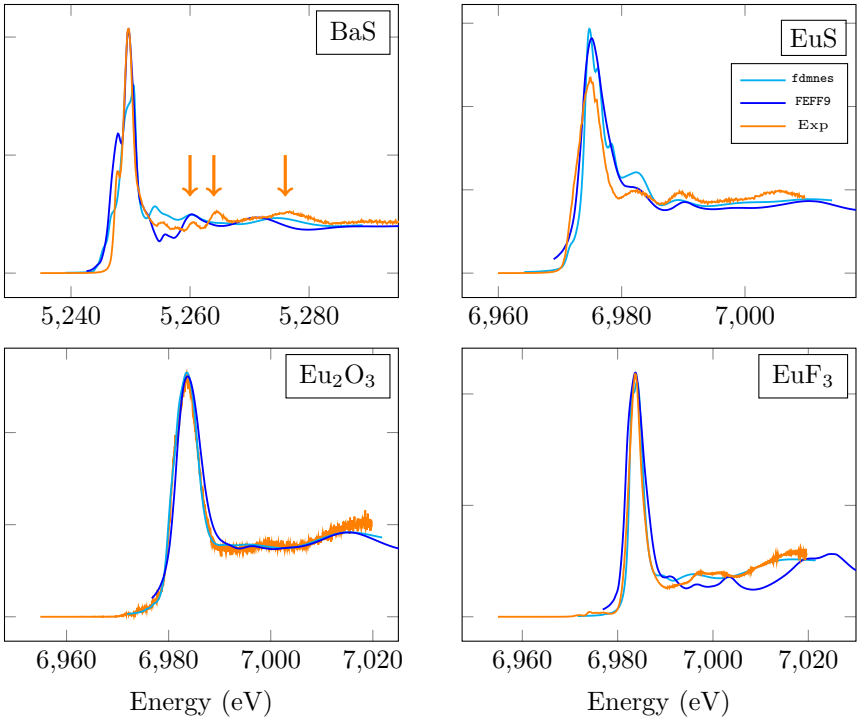

Figure 4.3: `FEFF9` (dark blue) and `fdmnes` (light blue) results for the different reference samples. Experimental data is in orange.

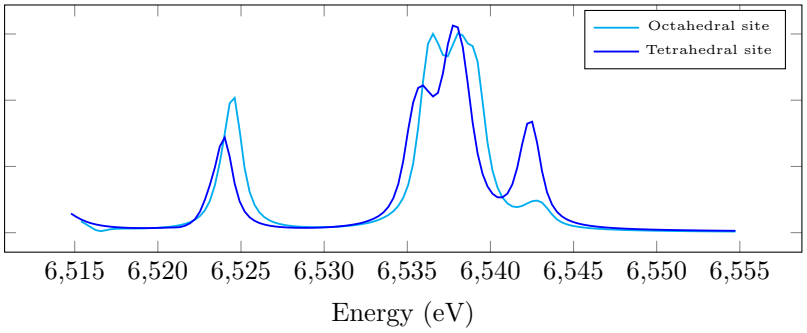

Figure 4.4: XES for the two different sites in Mn_3O_4

Table 4.1: Ionization of each atom from `FEFF9` calculations. The values show the net charge transfer within the radius of the neutral atom.

Compound	Eu	Ba	S	F	O
BaS		0.26	-0.36		
EuS	0.453		-0.251		
EuF_3	0.73			-0.225	
Eu_2O_3	0.537				-0.441

The calculation for EuS (top right in Figure 4.3) seems to be the one yielding the best results, especially from `FEFF9`. After a shift (around 3 eV) both the white-line and the following features are reasonably well aligned.

Concerning the comparison with `fdmnes` , there is an overall agreement in the number and position of peaks detected for EuS, Eu_2O_3 and to a less extent for BaS. The intensity is what is often not correct, both between the two software and between the experimental and simulated spectra. All the calculations from `fdmnes` have been run with the finite difference method and, in theory, should yield a more precise result at least in the energy position of the peaks (since those depend on the final state calculation in which `fdmnes` should excel). A huge improvement in quality, unfortunately, is not observed.

Charge transfer values are calculated automatically by `FEFF9` at each SCF iteration. These numbers represents the amount of positive charge that the algorithm transfers inside the atom by the end of the calculation, in order to have a reasonable picture of the crystal. Thus, a positive number like 0.5 means that half an electron has left the atom; this values are smaller than the formal oxidation state and this is what actually happens in atomic species, as it is very hard to remove a charge of 2 or 3 full electrons. Each one of the calculation converged successfully (with a variable number of iterations) and the resulting values are shown in Table 4.1.

Apparently, the total charge within the unit cell is not conserved, but with `FEFF9` thinking in terms of an infinite crystal is misleading. The software considers a spherical cluster of atoms centred on the absorber and the number of atomic species is not exactly representative of the stoichiometry due to boundary cuts. Nonetheless, the values appear reasonable and are consistent with the electro-negativity of each atom. Moreover, Eu is more oxidized when its formal configuration is 3+ (rather than 2+) and loses more charge when paired with F rather than O.

For Manganese, Mn_3O_4 was the only one studied and owes its choice to the local symmetry of the metal: the coordination with the Oxygen is the same as for the doping site in BAM:Mn. Unfortunately, no experimental data is available and the comparison is limited to the common features with simulated XANES and vtc XES for Mn in BAM. Mn_3O_4 has the advantage that half of the Manganese atoms occupies tetrahedral sites while the other half occupies octahedral sites. Performing calculations with the two kind of atoms as absorber, shows the effect that the coordination number has on the emission spectrum.

In Figure 4.4 the most visible difference is in the rightmost peak, that, in the Octahedral Manganese, has much lower intensity. This difference comes from the d DOS of Mn: the d electron occupancy of the tetrahedral and octahedral

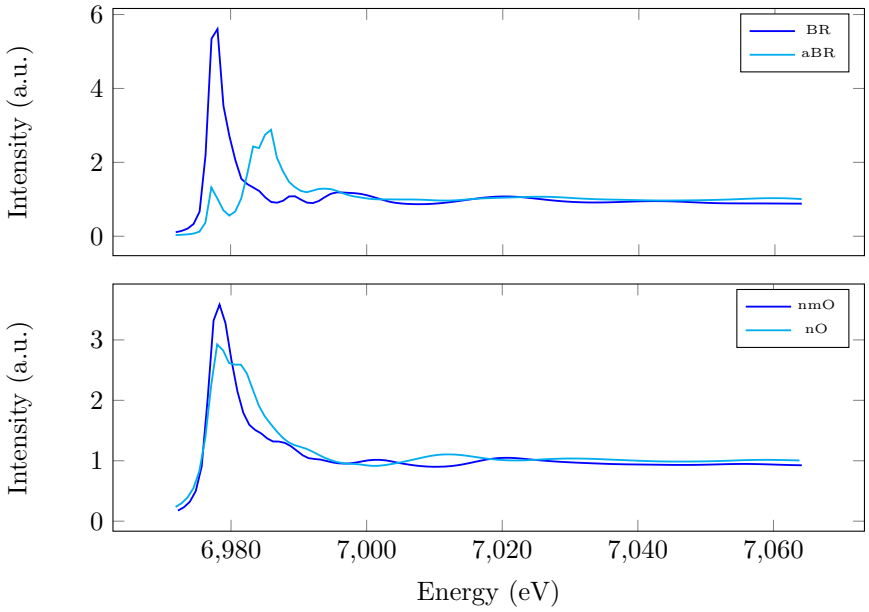

Figure 4.5: Simulations from `FEFF9` for the four different sites within the unit cell.

site is, respectively, 7.188 and 6.934; these numbers are due to the effect of six (rather than four) surrounding Oxygen. The higher pull of the electronegative atoms reduces the charge inside the radius of the fluorescent Manganese and the first states to be emptied are those nearer the Fermi level, i.e. those at higher energies. Lacking charge, these states cannot be any more an efficient source of radiative decay and the corresponding peak loses intensity.

4.2.2 Different sites for the Europium

The four plots in Figure 4.5 show the results from calculations for the four different Eu sites which are indicated in literature as stable in the conduction layer. It appears that the site called nmO (near-middle-Oxygen) does not differ significantly from the classical BR position. Therefore, it would be not easy to identify its contribution in the experimental spectra.

The spectrum from the nO position shows a second peak after the edge and this feature would be easily detected by the instrumentation in use at the beamline. The fact that it is not visible in the experimental spectra is proof that the nO site is not occupied.

The simulation for the aBR site shows a distinct feature: there is an intense pre-peak about 10 eV before the edge, a value that is consistent with the distance between the two peaks seen in the annealed and damaged BAM (Figure 3.1). This would suggest that in the final condition of the Eu doped BAM there is a change in position for the Europium.

This same spectrum shows two peaks at the edge (at 6983 eV and at 6985 eV). This is a feature not found in the experimental data and in the simulation is due to the choice of a negative imaginary part in the potential: this parameter reduces the core-hole lifetime and thus the amount of convolution performed on

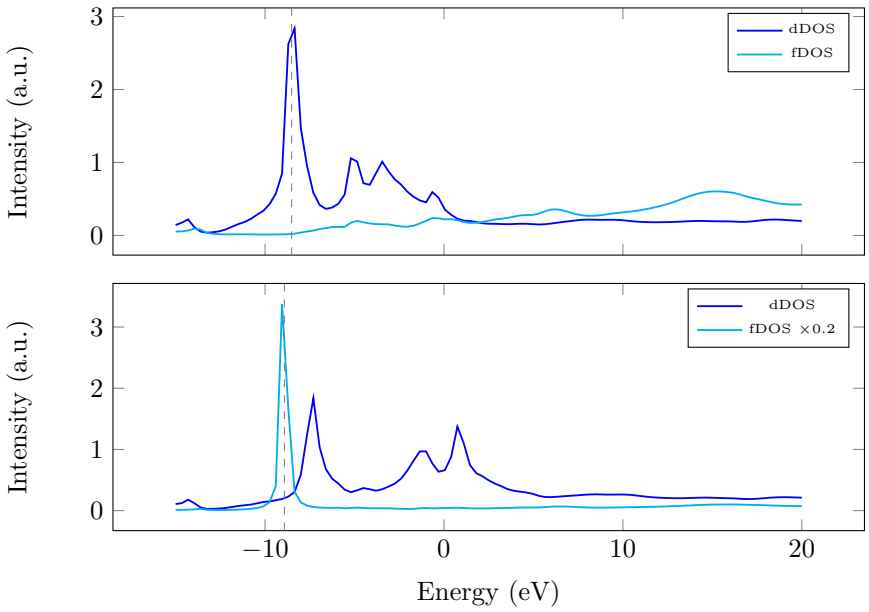

Figure 4.6: Comparison between the d and f orbitals when adding the card `UNFREEZEF` (top plot is without card and bottom plot is with card.). The Fermi level is indicated by the dashed grey line.

the density of states. A study of the density of states assigns the physical origin of the double peak to the d-DOS of Europium and the same can be said for the pre-peak (at 6977 eV). An additional proof for this assertion comes from the fact that `FEFF9` allows the user to choose which orbitals take part in the scattering process and when the d orbitals are not taken into account, all the peaks are merged into one.

Unfortunately, the relative intensity between the two peaks does not match the experimental one and different input files for the software did not lead to more satisfying outcomes. This particular result was obtained thanks to the card `UNFREEZEF`, whose effect is to compel the software to calculate the f density of states self-consistently (the use of this card does not change significantly the other calculations). By looking at the density of states (see Figure 4.6) from two calculations with and without this card, it is possible to see that the effect of the f orbitals is to push at higher energies the d states with a splitting that is wider than the following convolution (and thus remains visible in the spectrum).

After this brief discussion, unfortunately, the conclusion about the position of the Eu atom is still uncertain: the existence of the pre-edge (that is observed both in the measured and simulated spectra) leads us to rely on the simulations and say that there is a movement to the aBR site; on the other hand, there are also features that are not consistent with the experimental spectrum (see the comparison in Figure 4.7 top) and, being characteristic of this site, lead to the opposite conclusion. For example, the two peaks on the white-line and the intensity of the latter are among these peculiarities. Furthermore, the simulation identifies another less intense peak at 6993 eV that is not present at all in the spectrum from the laboratory.

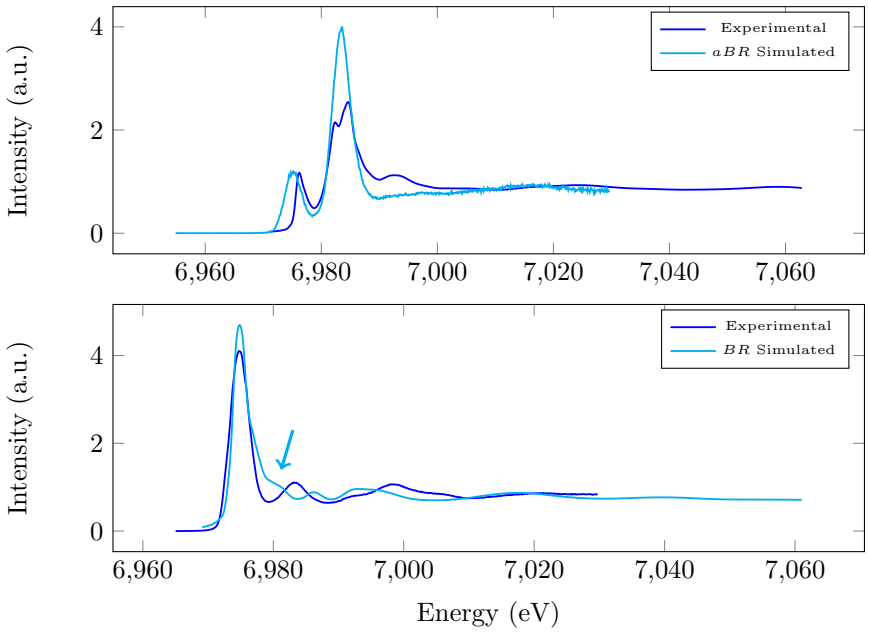

Figure 4.7: Top: comparison between an annealed BAM:Eu sample and the simulation for the aBR site. Bottom: comparison between the fresh sample and the simulation for the BR site.

Another interesting feature of the aBR simulation is the charge transfer values calculated for the Europium: with and without the `UNFREEZEF` card the values are, respectively, -0.790 and 0.092. These two numbers represents a reduced or neutral atom, while the expected phenomenon is an oxidation. This weights even more on the unreliability of the aBR simulation.

The simulation for the BR site (Figure 4.7 bottom) suffers from the same problem pointed out also for the calculations on references: some features seem to be identified, but their position is not correct. What cannot be assigned to any experimental peak is the shoulder on the high-energy side of the white-line (at 6983 eV, light-blue arrow); the not-so-good agreement with real data even for the most accepted position undermines the reliability of the simulations from `FEFF9` . While the odd results for the other more exotic sites could be assigned to a non-relaxed structure, the same cannot be said for this case. Diffraction studies show that the substitution from Barium to Europium is not followed by significant structural changes in the unit cell; thus, using this data, a more accurate simulation would have been expected and lack of quality should not be addressed to the atomic positions.

4.2.3 Oxidation state of Barium

Barium, surely fixed in the BR site, is taken as a reliable detector for what happens in the conduction (or mirror) layer. Besides the measurements concerning the irradiation damage, others were carried out to see if the atom is really sensitive to the presence of a dopant. This data is plotted in Figure 4.8,

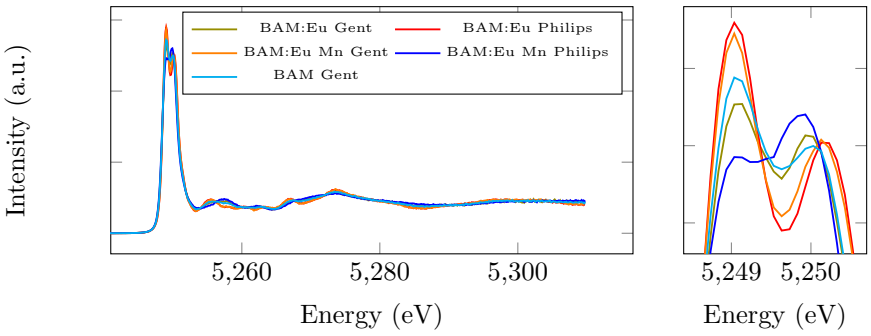

Figure 4.8: Barium L_{III} edge XANES

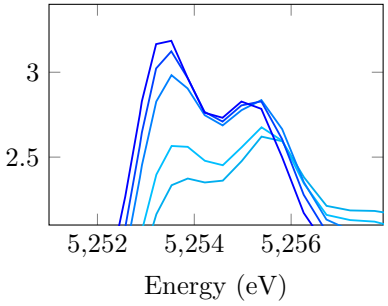

Figure 4.9: Ba L_{III} edge simulation for different Ba-O bond distances.

Table 4.2: Values from the charge transfer calculation for Ba and O.

Distance (Å)	Ba	O
2.5	0.487	-0.329
2.55	0.471	-0.328
2.6	0.572	-0.327
2.65	0.555	-0.329
2.7	0.534	-0.331

where also the differences in the white-line are high-lightened.

The calculations (a particular is shown in Figure 4.9) have been obtained considering a variable distance of the six surrounding Oxygen from the absorbing Ba. This was done in order to simulate a change in the oxidation state of the absorber, a phenomenon that is correlated to a shortening of the bond with the neighbouring electro-negative atoms (see, for example, the bond-valence method). The original distance found in the crystallographic file is 2.8 Å and the bond length evaluated in the calculations ranges from 2.5 to 2.7 Å. A shift of 0.3 Å is not small and would be readily detected in an EXAFS analysis: this kind of data is not available, but the entity of the movement compel us to look at the results with some caution.

A phenomenon similar to what is found experimentally is seen in the white-line: with respect to the bond distance, one of the two peaks diminishes in intensity in favour of the other. This suggests that what is seen in the data from the beamline is due to the movement of surrounding Oxygen and not to the presence or absence of some dopant in the mirror layer.

The calculation of charge transfer values does not yield a monotonous trend with respect to the bond length (Table 4.2). Ba seems to be subject to oxidation, but the lost charge is not transferred to the neighbouring Oxygen, whose electron charge does not appear to change. This undermines the interpretation that an oxidation of Ba follows the movement of the ligands.

Again, having reproduced this trend with a calculation is not a proof that

the Oxygen shift is really happening. The doubts arise primarily from the fact that the proposed movement is not small and a detailed analysis of a Barium EXAFS would surely give more insight on the topic.

Other calculations have been performed changing the position of Europium in the unit cell and, as a results, differences in the intensity, but not the shape, of the white-line are detectable. This suggests that the Barium would be indeed able to detect a structural change in the mirror layer and supports the hypothesis presented in Paragraph 4.2.2 about the Eu position that there is no movement. Instead, what could be said is that the atoms in the mirror layer are an easy target of oxidation, probably because the empty space in that region of the crystal allows small position shifts for the Oxygen.

4.2.4 Local symmetry around Manganese

The nominal position for Manganese is in the spinel block with tetrahedral coordination. The simulations from `FEFF9` help understanding which of the orbitals in the v.t.c XES (Figure 4.10, top) are contributing to each peak. This is possible thanks to the projected density of states, automatically calculated by the software, that allows to associate an absorption peak to a transition toward an unoccupied state.

The experimental and simulated spectra are shown in Figure 4.10, where it is possible to see that the number and, to a smaller precision, position of peaks is correct. Thanks to the middle and bottom plot in the same Figure, it becomes clear that the lone peak at -28 eV is due to the surrounding Oxygen's s orbitals while the one on the opposite side of the spectra is due mostly to Manganese p and d orbitals. It appears that p states from both atomic species are hybridized to give the two central peaks and that Oxygen gives a small contribution to the rightmost peak.

In order to study the sensitivity of Manganese to the changes in the mirror layer, simulations with co-doped BAM have been performed. It is found that the presence of Eu in place of Barium does not affect at all the emission spectrum: the spectra for BAM:Mn and BAM:Mn,Eu are exactly identical, hinting that no change whatsoever happens in the spinel block after the cation substitution (although v.t.c. XES is sensitive mostly to the metal and the ligands and the mirror layer could already be too far).

In order to exclude the possibility of Manganese occupying a different site, the case of substitution of an octahedral site has been tested. These sites are still in the spinel block and are occupied by Aluminium and rarely by Magnesium. Their occupancy has been reported as a less probable event [26] and thus little effort has been put in the study. The result shows that, in this case, the rightmost peak is absent while the others remain unchanged, not giving a direct way to rule out the possibility of co-existence of octahedral and tetrahedral sites. The explanation for this missing peak is the same as the one given for the emission spectra of Mn_3O_4 in Section 4.2.1.

Manganese XANES measurements show no dependence neither on doping nor on irradiation. In this case the absorber is 6 Å from the BR site, a distance that is already enough to dampen the possible effects of a dopant on the spectra. Concerning the simulation from `FEFF9` (Figure 4.11), unfortunately, the result is not very good: the software identifies only a limited number of peaks, and most of them have the wrong intensity. The only common feature with the

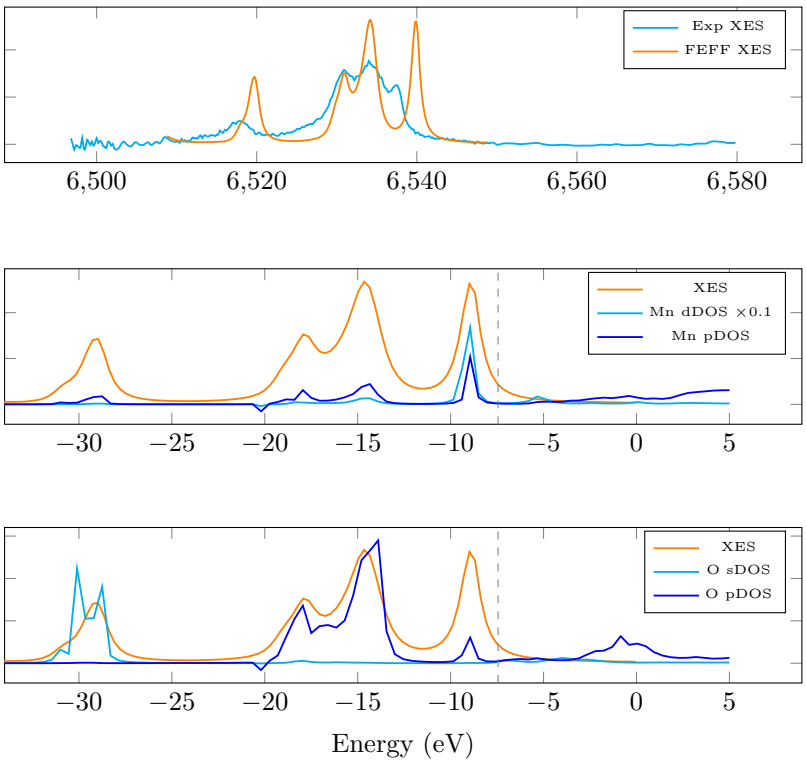

Figure 4.10: Top: Comparison between experimental and simulated XES. Middle: projected density of states for the Manganese. Bottom: Projected density of states for the four surrounding Oxygen. The gray dashed line represents the position of the Fermi level.

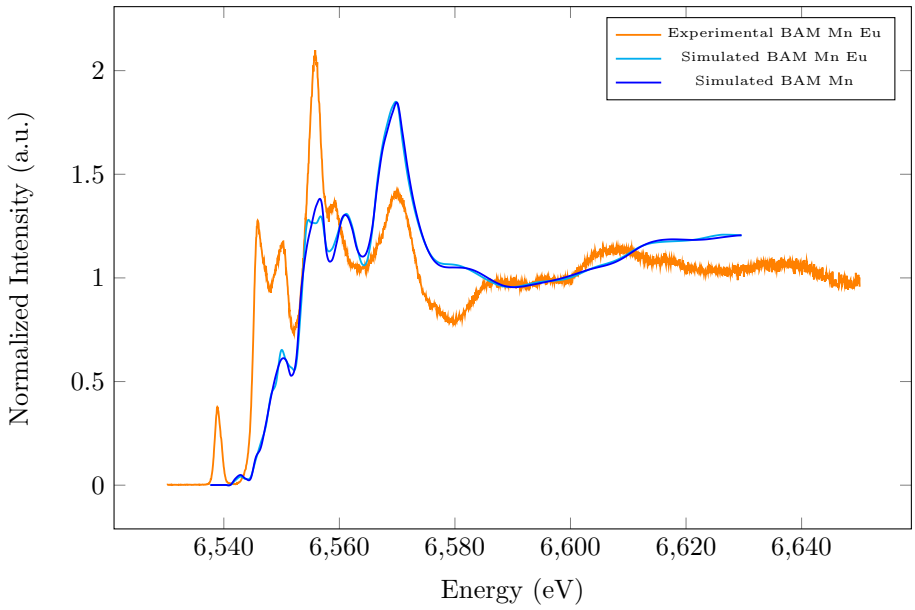

Figure 4.11: XANES Mn K edge: experimental data and simulation from `FEFF9` .

experimental data is the absent dependence on the co-doping. Better results for the Mn XANES have been achieved with `fdmnes` and will be discussed in the next Paragraph.

4.2.5 Results from `fdmnes` for BAM

Throughout the work, the calculations from `FEFF9` have been easier to obtain and to interpret and this is the reason why they have been presented before. Moreover, when Europium was considered as a dopant in the BAM structure, `fdmnes` had problems reaching convergence in the SCF calculation. In the following plots a comparison with the results from `fdmnes` is shown in order to see if there is coherence between the two software.

A brief discussion on the reference sample has already been carried out and, therefore, this section will deal only with luminescent BAM.

Here (Figure 4.13), the simulations are less consistent: among the four different sites for the Europium atom, only the BR position gives some sort of qualitative agreement but, even in this case, `fdmnes` does not identify the features beyond the white-line. Considering the other three sites, the disagreement could be another proof that the idea of a position shift for the Europium atom is rather unreasonable. In particular, in the aBR case, although two peaks are actually calculated, their relative intensity is the opposite as in `FEFF9` and the distance between them is too small. But then again, convergence in the SCF was not reached, so the electronic structures upon which the spectra are calculated are not really accurate.

For the Barium L edge, `fdmnes` is not able to identify the double peak that in Paragraph 4.2.3 has been assigned to the oxidation state. Instead, like in `FEFF9` , there is a shoulder to the white-line at 5253 eV (blue arrow), but no

peak between it and the hump at around 5270 eV.

There is agreement between the simulations for the Manganese emission spectroscopy, apart for a small peak at 6131 eV. Unfortunately, the two central peaks are still off by some eV with respect to the experimental spectrum.

The calculation where `fdmnes` shows a better result is the Manganese XANES K edge (Figure 4.12): here all features are identified and are reasonably accurate both in position and intensity (only the two peaks at 6550 eV are slightly underestimated by the software). The analysis of the density of states shows that all the peaks are due to the p projected density and gives some hints on the interpretation of the pre-peak. The p and d densities show two sharp peaks at that particular energy, suggesting that it is due to transition towards hybridized $p-d$ orbitals. For this calculation the result given by `fdmnes` for the Fermi level was not correct: it was too high and the pre-peak was not taken into account in the convolution; therefore, to obtain the correct result, it has been manually moved to -9 eV.

To summarize, a greater level of quality was expected, at least in terms of common features between the results from the two codes. The complexity of the crystal structure makes the spectra harder to simulate, but this does not explain, for example, the huge difference in time required to reach convergence in the SCF calculation. While `FEFF9` usually ends the potential calculation within 20 cycles, `fdmnes` requires more than 300 iterations and often this is not sufficient (the code finishes with an energy difference between cycles 4 or 5 orders of magnitude greater than the set threshold).

This fact justifies the inaccurate results from the second software and could show a sensitivity to non-relaxed crystal structure that is not present in `FEFF9` . It is possible that `fdmnes` has problems calculating the potentials for the aBR, nO and nmO sites due to the fact that a substitution of Europium in these places is not physically correct without an optimization of the surrounding structure.

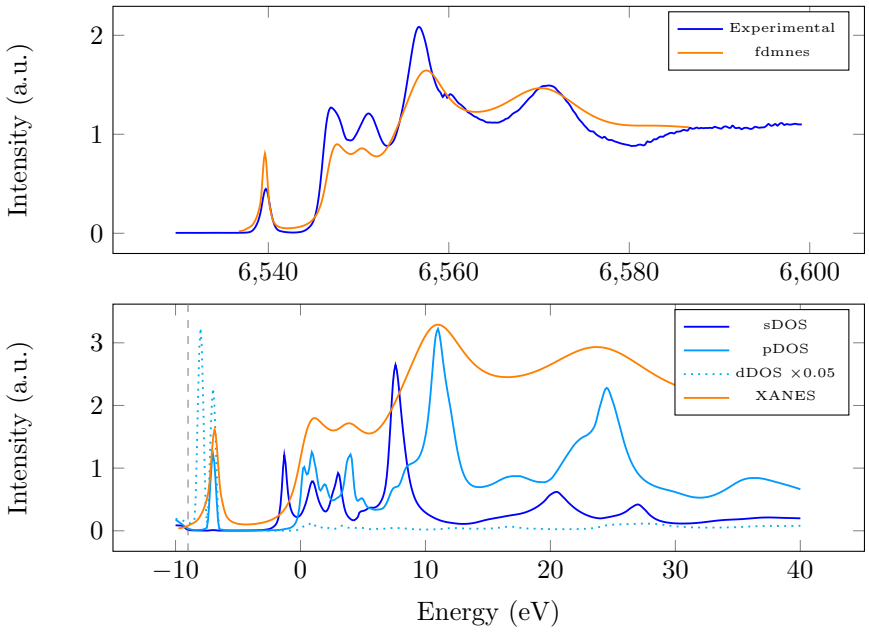

Figure 4.12: Top: comparison between experimental and simulated spectra from `fdmnes` . Bottom: projected density of states for the Manganese. The gray dashed line represents the position of the Fermi level.

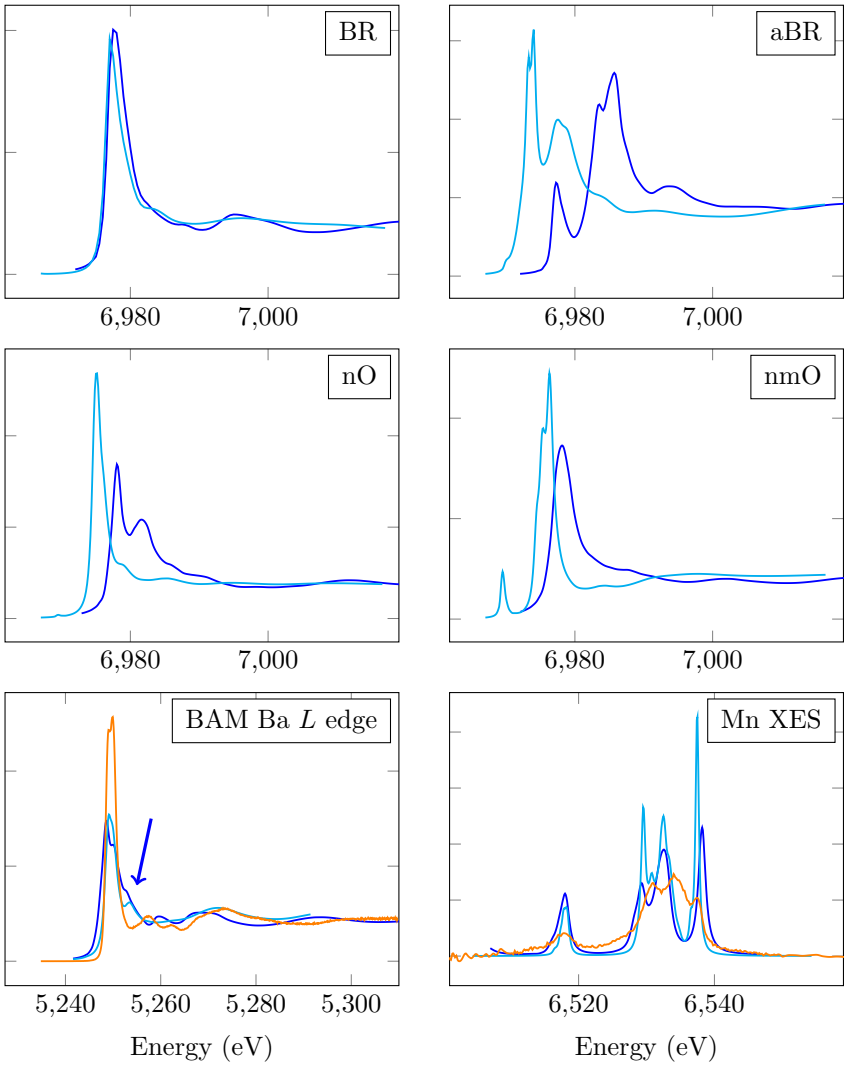

Figure 4.13: `FEFF9` (dark blue) and `fdmnes` (light blue) results for the material of interest. Experimental data is in orange.

Chapter 5

Conclusions

Conclusions for the present work can be associated to three different topics: the application of PCA as a statistical tool, the understanding of doped BAM structure and the comparison between two software (`FEFF9` and `fdmnes`).

PCA has proven to be not very useful by itself, since it does not offer a way to uniquely determine the physically meaningful matrices in which the dataset is decomposed. Besides, the IE and IND parameter used to evaluate the number of factors remain quite ambiguous, even if the mathematical formulation gives them an objective appearance.

The algorithm of Target Transformation (TT) and Non Negative Matrix Factorization (NNMF) give more interesting results, but PCA is not strictly a prerequisite for their application; as a matter of fact, often, the number of components estimated from an educated guess does not differ from the output of a PCA. Indeed, the application of TT provides a reason to believe that annealing and irradiation yield similar effects on the sample; at the same time, NNMF gives an independent way to obtain underlying factors in a dataset and the results are consistent with the fresh and damaged reference spectra.

Concerning the material itself, the crystallographic structure found in literature has proven to be coherent with the results obtained from X-Ray analysis. As there were few doubts on the atomic positions, this is mostly an assessment on the reliability of XANES to probe the local structure and symmetry around the absorbing atom.

Oxidation has been identified as the most plausible cause for the loss in luminescence, following both annealing and irradiation, and no proofs of a possible movement of Europium within the mirror layer have been found. The valence state change from Eu^{2+} to Eu^{3+} disrupts the energy transfer between the host material and the dopant: this happens due to a shift in the energy position of Eu^{3+} states and causes the drop in light emission efficiency.

Oxidation also seems to take part in the changes in the Ba L edge white-line. This suggests that the mirror layer itself is not very resistant to the movement of Oxygen and a relaxation of the crystal structure might be the physical cause of the intensity shift. The conduction layer is a very mobile environment and could allow for the inclusion and movement of Oxygen from the atmosphere even at room temperature. The most obvious way to test this assumption would be an

EXAFS at the Barium edge, in order to evaluate the positions of the surrounding atomic species.

Software simulations do not help in considering the movement of the dopant as a valid explanation: there is not enough consistence in the results between the two software to consider the output reliable. This could either point towards the fact that the sites local structure is not correct or to the fact that calculations become less precise when considering atoms as heavy as Europium.

The latter seems to be the case of `fdmnes`, given the problems found when performing SCF calculation with the presence of Eu (even for some references, like EuS and Eu_2O_3). `FEFF9`, instead, has not given this kind of problems and the calculations converged smoothly.

Concerning the meaning of the successfully terminated simulations, it seems that the results are limited to a qualitative agreement. Only Manganese XANES and XES are very well represented by `fdmnes` . Unfortunately, a better matching between the features both in terms of energy position and intensity has not been achieved and the cause probably lays in the calculation of the final states.

Probably, by using more advanced and time consuming DFT techniques, more accurate electronic structures could be calculated. Spectra based on these results could yield a better understanding of the experimental features found in the measurements.

Another improvement in the simulation could be expected if a relaxed structure is considered. The inclusion of Europium in BAM does not change the atomic position, but what happens with a possible movement of the atom is not exactly clear. Perhaps a slight change in the position of the atoms surrounding the aBR, nO and nmO sites could add to the simulation the reliability that, for now, seems to be missing.

Bibliography

[1] Matthias Bauer. "HERFD-XAS and valence-to-core-XES: new tools to push the limits in research with hard X-rays?" In: *Physical Chemistry Chemical Physics* 16.27 (2014), pp. 13827–13837.

[2] U Bergmann et al. "Chemical dependence of interatomic X-ray transition energies and intensities–a study of Mn Kβ and Kβ 2, 5 spectra". In: *Chemical physics letters* 302.1 (1999), pp. 119–124.

[3] G Bizarri and B Moine. "On $BaMgAl_{10}O_{17}$:Eu^{2+} phosphor degradation mechanism: thermal treatment effects". In: *Journal of Luminescence* 113.3 (2005), pp. 199–213.

[4] G Bizarri and B Moine. "On the role of traps in the $BaMgAl_{10}O_{17}$: Eu^{2+} fluorescence mechanisms". In: *Journal of luminescence* 115.1 (2005), pp. 53–61.

[5] O Bunău and Yves Joly. "Self-consistent aspects of x-ray absorption calculations". In: *Journal of Physics: Condensed Matter* 21.34 (2009), p. 345501.

[6] L Campbell et al. "Interference between extrinsic and intrinsic losses in x-ray absorption fine structure". In: *Physical Review B* 65.6 (2002), p. 064107.

[7] Paolo Carra, Michele Fabrizio, and BT Thole. "High resolution x-ray resonant Raman scattering". In: *Physical review letters* 74.18 (1995), p. 3700.

[8] Brennan Dawson et al. "Mechanisms of VUV damage in $BaMgAl_{10}O_{17}$: Eu^{2+}". In: *Chemistry of materials* 16.25 (2004), pp. 5311–5317.

[9] FMF De Groot, MH Krisch, and J Vogel. "Spectral sharpening of the Pt L edges by high-resolution x-ray emission". In: *Physical Review B* 66.19 (2002), p. 195112.

[10] Qian Du, Ivica Kopriva, and Harold Szu. *Investigation on constrained matrix factorization for hyperspectral image analysis*. Tech. rep. DTIC Document, 2005.

[11] Martin J Fay et al. "Determination of the Mo surface environment of Mo/TiO_2 catalysts by EXAFS, XANES and PCA". In: *Microchimica Acta* 109.5-6 (1992), pp. 281–293.

[12] Erik Gallo and Pieter Glatzel. "Valence to Core X-ray Emission Spectroscopy". In: *Advanced Materials* 26.46 (2014), pp. 7730–7746.

[13] Pieter Glatzel and Amélie Juhin. "X-ray Absorption and Emission Spectroscopy". In: *Local Structural Characterisation*. John Wiley & Sons Ltd, 2013, pp. 89–171. ISBN: 9781118681909. DOI: 10.1002/9781118681909.ch2. URL: http://dx.doi.org/10.1002/9781118681909.ch2.

[14] Pieter Glatzel et al. "Hard x-ray photon-in-photon-out spectroscopy with lifetime resolution–of XAS, XES, RIXSS and HERFD". In: (2007).

[15] Pieter Glatzel et al. "Reflections on hard X-ray photon-in/photon-out spectroscopy for electronic structure studies". In: *Journal of Electron Spectroscopy and Related Phenomena* 188 (2013), pp. 17–25.

[16] K Hämäläinen et al. "Elimination of the inner-shell lifetime broadening in X-ray-absorption spectroscopy". In: *Physical review letters* 67.20 (1991), p. 2850.

[17] D Heslop, T Von Dobeneck, and M Höcker. "Using non-negative matrix factorization in the "unmixing" of diffuse reflectance spectra". In: *Marine Geology* 241.1 (2007), pp. 63–78.

[18] Ichiro Hirosawa et al. "Influence of x-ray irradiation on doped europium in $BaMgAl_{10}O_{17}$ studied by x-ray absorption fine structure and x-ray diffraction". In: *Journal of the Society for Information Display* 13.8 (2005), pp. 673–678.

[19] Philip K Hopke. "Target transformation factor analysis". In: *Chemometrics and intelligent laboratory systems* 6.1 (1989), pp. 7–19.

[20] Harold Hotelling. "Analysis of a complex of statistical variables into principal components." In: *Journal of educational psychology* 24.6 (1933), p. 417.

[21] Brandon Howe and Anthony L Diaz. "Characterization of host-lattice emission and energy transfer in $BaMgAl_{10}O_{17}$:Eu^{2+}". In: *Journal of luminescence* 109.1 (2004), pp. 51–59.

[22] Marie-Pierre Isaure et al. "Quantitative Zn speciation in a contaminated dredged sediment by μ-PIXE, μ-SXRF, EXAFS spectroscopy and principal component analysis". In: *Geochimica et Cosmochimica Acta* 66.9 (2002), pp. 1549–1567.

[23] Zhang Jia-Chi, Zhou Mei-Jiao, and Wang Yu-Hua. "Photoluminescence degradation mechanism of $BaMgAl_{10}O_{17}$:Eu^{2+} phosphor by vacuum ultraviolet irradiation". In: *Chinese Physics B* 21.12 (2012), p. 124102. URL: http://stacks.iop.org/1674-1056/21/i=12/a=124102.

[24] Ian Jolliffe. *Principal Component Analysis*. Wiley Online Library, 2002.

[25] Y Joly. "X-ray absorption near-edge structure calculations beyond the muffin-tin approximation". In: *Physical Review B* 63.12 (2001), p. 125120.

[26] Kwang-Bok Kim et al. "Structural and optical properties of $BaMgAl_{10}O_{17}$:Eu^{2+} phosphor". In: *Chemistry of Materials* 14.12 (2002), pp. 5045–5052.

[27] Manfred Otto Krause and JH Oliver. "Natural widths of atomic K and L levels, Kα X-ray lines and several KLL Auger lines". In: *Journal of Physical and Chemical Reference Data* 8.2 (1979), pp. 329–338.

[28] Juliette Lambert et al. "Searching for the dopant ion in Eu^{2+}-activated $BaMgAl_{10}O_{17}$ phosphor with synchrotron diffraction". In: *Journal of Luminescence* 128.3 (2008), pp. 366–372.

[29] Daniel D Lee and H Sebastian Seung. "Algorithms for non-negative matrix factorization". In: *Advances in neural information processing systems*. 2001, pp. 556–562.

[30] Bitao Liu et al. "The reduction of Eu^{3+} to Eu^{2+} in $BaMgAl_{10}O_{17}$:Eu and the photoluminescence properties of $BaMgAl_{10}O_{17}$:Eu^{2+} phosphor". In: *J Appl Phys* 106 (2009), pp. 053102–053107.

[31] Edmund R Malinowski. *Factor analysis in chemistry*. Wiley, 1991.

[32] B Moine and G Bizarri. "Rare-earth doped phosphors: oldies or goldies?" In: *Materials Science and Engineering: B* 105.1 (2003), pp. 2–7.

[33] CR Natoli. "Distance dependence of continuum and bound state of excitonic resonances in x-ray absorption near edge structure (XANES)". In: *EXAFS and Near Edge Structure III*. Springer, 1984, pp. 38–42.

[34] K Person. *On Lines and Planes of Closest Fit to System of Points in Space. Philiosophical Magazine, 2, 559-572*. 1901.

[35] Bruce Ravel. "A practical introduction to multiple scattering theory". In: *Journal of Alloys and compounds* 401.1 (2005), pp. 118–126.

[36] John J Rehr et al. "Parameter-free calculations of X-ray spectra with FEFF9". In: *Physical Chemistry Chemical Physics* 12.21 (2010), pp. 5503–5513.

[37] Thorsten Ressler et al. "Quantitative speciation of Mn-bearing particulates emitted from autos burning (methylcyclopentadienyl) manganese tricarbonyl-added gasolines using XANES spectroscopy". In: *Environmental science & technology* 34.6 (2000), pp. 950–958.

[38] Olga V Safonova et al. "Identification of CO adsorption sites in supported Pt catalysts using high-energy-resolution fluorescence detection X-ray spectroscopy". In: *The Journal of Physical Chemistry B* 110.33 (2006), pp. 16162–16164.

[39] MP Seah and WA Dench. "Quantitative electron spectroscopy of surfaces: a standard data base for electron inelastic mean free paths in solids". In: *Surface and interface analysis* 1.1 (1979), pp. 2–11.

[40] Jonathon Shlens. "A tutorial on principal component analysis". In: *arXiv preprint arXiv:1404.1100* (2014).

[41] Kee-Sun Sohn, Sang Sub Kim, and Hee Dong Park. "Luminescence quenching in thermally-treated barium magnesium aluminate phosphor". In: *Applied physics letters* 81.10 (2002), pp. 1759–1761.

[42] Moniek Tromp et al. "High Energy Resolution Fluorescence Detection X-Ray Absorption Spectroscopy: Detection of Adsorption Sites in Supported Metal Catalysts". In: *X-Ray Absorption Fine Structure–XAFS 13* 882 (2007), pp. 651–653.

[43] SR Wasserman. "The analysis of mixtures: application of principal component analysis to XAS spectra". In: *Le Journal de Physique IV* 7.C2 (1997), pp. C2–203.

[44] Jiachi Zhang et al. "The ultraviolet irradiation degradation of fluorescent lamp used $BaMgAl_{10}O_{17}$:Eu^{2+}, Mn^{2+} phosphor". In: *Journal of Luminescence* 132.8 (2012), pp. 1949–1952.